Inspired shape memory effect and superelasticity of ultra-light Gyroid TPMS lattice structures fabricated by laser powder bed fusion

Di Lin [a], Yunlong Ren[a], Siqi Wu[b], Mengying Chen[a], Hui Qiao[a], and Lei Yang [a, b*]

[a] *School of Transportation and Logistics Engineering, Wuhan University of Technology, Wuhan, China*

[b] *State Key Laboratory of Materials Processing and Die & Mould Technology, School of Materials Science and Engineering, Huazhong University of Science and Technology, Wuhan, China*

Abstract:

Ni-Ti shape memory alloys based on triply periodic minimal surface (TPMS) lattice structures are garnering increasing interest from researchers due to their significant potential for applications in bone tissue engineering. In this study, the Gyroid TPMS lattice structures with the extremely low volume fractions, ranging from 1% to 4%, were fabricated using the laser powder bed fusion (LPBF) technique. A comprehensive orthogonal experiment was performed to determine the optimal printing parameters and compare the manufacturing fidelity between parameters with high and low energy density. The findings indicated that the printing parameters of 220 W laser power, 1400 mm/s scanning velocity, 40 μm layer thickness, 70 μm hatch spacing with 56.12 J/mm^3 were deemed suitable, while the precision of manufacturing with high energy density parameters was inferior. Moreover, experimental analysis was conducted on the uniaxial compression mechanical properties, superelastic responses, and shape memory effects of ultra-light Ni-Ti Gyroid lattice structures. The finite element method was employed to illustrate the stress distributions and fracture mechanisms of these lattice structures. The result revealed that the ultra-light Ni-Ti Gyroid lattice structures exhibited outstanding superelastic properties, with a recoverable ratio of 93.65% for the structure with a VF of 3%, and remarkable shape memory effects, with recoverable ratios ranging from 98.99% to 99.80% at 8% compressive strains.

* Corresponding author: lei.yang@whut.edu.cn(L. Yang); zhangcong@whut.edu.cn(C. Zhang)

2. Introduction

Nickel-titanium (Ni-Ti) shape memory alloys (SMAs) have been increasingly crucial in biomedicine, aerospace, automobile, structural engineering and other fields owing to their excellent mechanical properties such as biocompability[1], unique superelasticity (SE) as well as shape memory effects (SME) [2] [3]. These SMAs have two diverse crystalline structures: the low-temperature stable phase, referred to as martensite (M), and high-temperature stable phase, known as austenite (A) [4]. The prevailing crystalline structures depend on temperature and external loading applied. When the austenite phase is subjected to stress within a certain temperature range, it undergoes a transformation to the martensite phase. Given that martensite cannot sustain itself without stress at these temperatures, it reverts back to austenite phase upon stress removal, thereby reversing the deformation. This phenomenon leads to a significant elastic response, known as superelasticity[5] [6] [7]. In addition, Ni-Ti alloys are capable of regaining their original shape through a reversible martensitic transformation, specifically from low-temperature martensite to high-temperature austenite. The deformation of the low-temperature martensite occurs via reorientation and detwinning of martensite lattice structure. Upon subsequent heating, the martensite transforms back to austenite, thereby recovering the original shape. This phenomenon is referred to as the shape memory effect of Ni-Ti alloys[8] [9] [10] [11]. Therefore, the SE and SME of Ni-Ti alloys can be obtained through applied loading and temperature transformation. Due to the characteristics of SE and SME, Ni-Ti alloys have found extensive applications in the field of biomedical implants. For example, a bone staple can be positioned across the two adjoining surfaces of a bone in a distinctive shape, and then recover to its intended shape due to the body heat[12]. However, the majority of research has been centered around solid Ni-Ti alloys, whose elastic modulus is nonetheless considerably higher than that of human bones. An excessively high elastic modulus can lead to the resorption of surrounding bones, a phenomenon known as the stress shielding effect, which can subsequently result in premature implant fractures and surgical failures[13]. Currently, the incorporation of porous structures is being considered as a potential strategy to lower the elastic modulus and enhance biocompatibility[14].

Over the years, Ni-Ti porous structures have been primarily produced using conventional techniques, such as powder metallurgy [15], combustion synthesis [16], hot isostatic pressing [17], vacuum arc remelting, vacuum induction melting and metal injection molding [18] [19] [20]. However, these fabrication methods fall short in achieving complex geometries, specific pore size, precise dimensional lengths, and customized mechanical behaviors. Moreover, the aforementioned techniques pose challenges in producing surgical bone implants with personalized morphology and hierarchical internal architecture[21]. However, in recent years, the swift advancement of metal-based additive manufacturing (MAM) techniques, such as laser power bed fusion (LPBF) and electron beam melting (EBM), has enabled the fabrication of highly precise porous metals with intricate external shapes and internal architectures. Additive manufacturing (AM) technology has been particularly beneficial in overcoming the poor workability of Ni-Ti alloys. Presently, through LPBF, Ni-Ti SMAs can be fabricated into 3D structures with complex geometrical configurations, as opposed to conventional geometries like tubes, rods, wires and sheets[22].

At present, many researchers are focusing on the study of Simple Cubic (SC) [23], Body-Centered Cubic (BCC) [24], and Octahedron structures [25], as the AM techniques allow for the fabrication of parts through layer-by-layer construction approach. However, these structures exhibit uneven and abrupt transitions near joints, leading to stress concentrations that can result in premature fractures under load [26]. Therefore, attention must be paid to issues of stress concentration and localized structural failure.

In recent times, to address the issues of stress concentration and brittle joints, a lattice structure based on the triply periodic minimal surface (TPMS), a unique surface with periodic geometric variations in three independent directions and a zero mean curvature radius, has been widely studied[27]. TPMS lattice structures not only offer superior manufacturing accuracy, but also exhibit a more uniform stress distribution under load compared to other kinds of lattice structures, such as BCC and octahedron lattices [28]. This is attributed to the distinctive characteristics of TPMSs, namely their continuous and smooth surfaces as well as zero curvatures. Furthermore, Saghaian et al. [29] found that it is feasible to reduce the Young's modulus of TPMS lattices by approximately 76% to 90% by altering the configuration and relative density of TPMS lattice structures. Moreover, research conducted by Maskery et al. [30] demonstrated that the Gyroid lattice structure displayed a threefold increase in energy absorption per unit mass compared to the BCC lattice structure, under a compressive strain of 50%. This suggests that the geometrical characteristics of TPMSs can significantly enhance the mechanical performance. Additionally, a TPMS lattice boasts a high specific surface area and superior mechanical performance, suggesting that human trabecular bones implanted with a TPMS lattice structure may exhibit improved tissue regeneration

performance [28]. Therefore, TPMS lattice structures are viewed as promising porous structures for surgical applicants, and when combined with Ni-Ti SMAs, they could potentially serve as biological bone substitutes[31].

Notably, the shape memory behavior of the Ni-Ti lattice structure tends to increase as its volume fraction decreases[3]. A decline in volume fraction (VF) implies a reduction in the overall weight of the structure, making lightweight Ni-Ti lattice structures particularly relevant for applications in the aerospace and automobile industries. However, most research to date has focused on Ni-Ti lattice structures with a VF of above 5%. For instance, Jin [32] et al. investigated a Ni-Ti lattice sample with VF of 30%. Zhu [20] et al. researched Ni-Ti porous structures with 20 and 40 vol%. Sun [33] et al. studied Ni-Ti TPMS lattice structures with VF of 12.5%. Jin [3] et al. investigated multicell interlacing Ni-Ti TPMS lattice structures with VF of 20% and Yang [34] et al. systematically studied the effect of volume fraction ranging from 7% to 20% on Mechanical properties of Ni-Ti TPMS lattices. However, relative studies on lattice structures with extremely low VF nonetheless lacks. Therefore, in this work, the SE and SME of ultra-light Ni-Ti Gyroid lattices with 1%, 2%, 3% and 4% of VF, respectively were systematically investigated.

2. Methodologies

2.1. Design and fabrication of TPMS lattice structures

TPMS lattice structures, with varying volume fractions (VFs) were designed and modelled using trigonometric implicit functions in MATLAB (Mathworks Inc., USA). The mathematical equation governing the Gyroid TPMS lattice structure is as follow:

$$\Phi_G: \sin\left(\frac{2\pi}{a} \cdot x\right) \cos\left(\frac{2\pi}{a} \cdot y\right) + \sin\left(\frac{2\pi}{a} \cdot y\right) \cos\left(\frac{2\pi}{a} \cdot z\right) + \sin\left(\frac{2\pi}{a} \cdot z\right) \cos\left(\frac{2\pi}{a} \cdot x\right) - t \quad (1)$$

In this equation, the parameters a and t respectively determine the unit cell size and the volume fraction of the TPMS lattices[35], while (x, y, z) represent the spatial coordinates of specific points within TPMS lattices. However, when the volume fraction of a TPMS lattice structure falls below a certain threshold, there is a classical problem called pinch-off problem. According to previous work[36], an optimization Gyroid TPMS function was introduced. The optimized function is shown below,

$$\Phi_{G\text{-Opt}}: c \cdot \Phi_G - d \cdot \left[\sin\left(3 \cdot \frac{2\pi}{a} \cdot x\right) \cos\left(3 \cdot \frac{2\pi}{a} \cdot y\right) + \sin\left(3 \cdot \frac{2\pi}{a} \cdot y\right) \cos\left(3 \cdot \frac{2\pi}{a} \cdot z\right) + \sin\right.$$

$$\left.\left(3 \cdot \frac{2\pi}{a} \cdot z\right) \cos\left(3 \cdot \frac{2\pi}{a} \cdot x\right)\right] \quad (2)$$

In this equation, constants c and d regulate the value of struct diameter of the Gyroid lattices. Take Gyroid TPMS as an example, as presented in Fig. 1(a), the cubic space is participated into two non-intersecting, intertwined sub-spaces with open cavities by a two-sided surface known as the Gyroid surface. When each sub-space is filled with solid material, a skeleton-based Gyroid TPMS scaffold is formed, with the Gyroid

surface serving as the solid-void interface. TPMS structures can be generated by repeating the TPMS unit-cells in the X, Y and Z directions. In this study, a set of ultra-light Gyroid TPMS lattices was constructed as shown in Fig.1(b). The entire set of samples was designed with the same total dimensions of 40 mm × 40 mm × 40 mm and the identical unit-cell size (a) of 10 mm but different volume fractions of 1%, 2%, 3% and 4%.
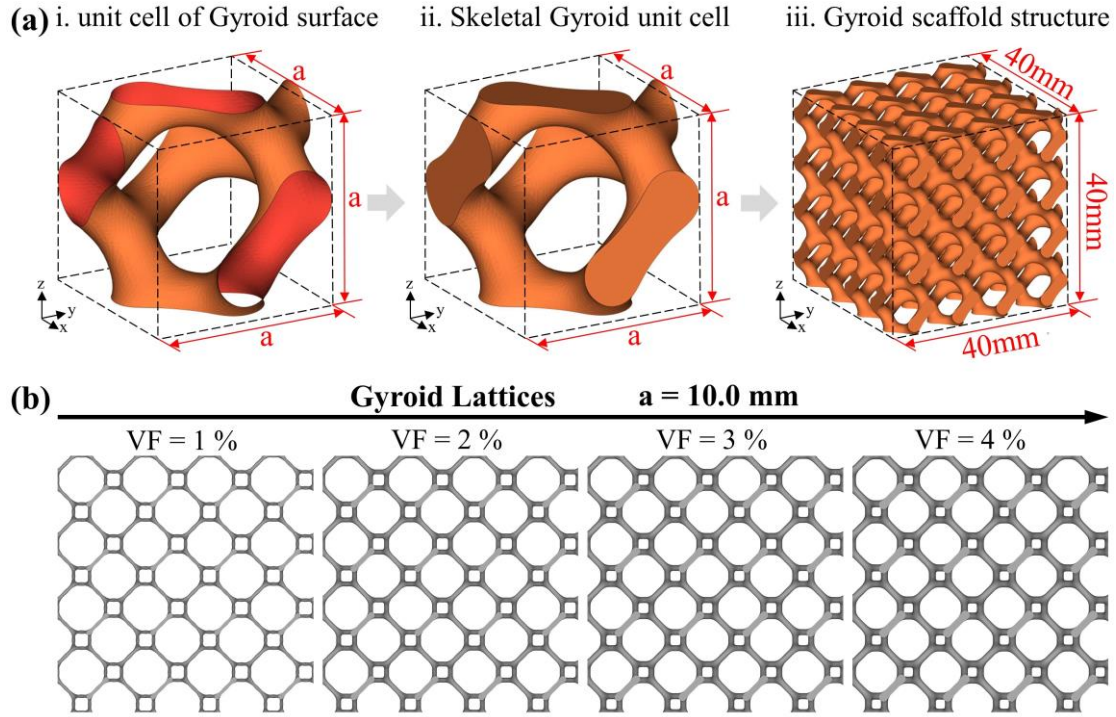

Fig. 1. (a) Schematics of unit cell of Gyroid surface, skeletal Gyroid unit cell, and skeletal Gyroid TPMS lattice structure. Front views of designed models of different types of TPMS lattice structures: (b) Gyroid lattices.

2.2 Materials and fabrication process

The Ni-Ti powder utilized in this study was produced using electrode induction melting gas atomization technology (AVIMETAL Additive Manufacturing Technology (Beijing) Co., Ltd). The chemical composition of as-received Ni-Ti powder was measured to be $Ni_{50.8}Ti_{49.2}$ by EMPA-8050G electron prove micro-analyzer (EPMA) (Shimadzu, Japan). The morphology of the Ni-Ti powder was examined using a Quanta650 FEG scanning electron microscope (SEM) (FEI, America). As represented in Fig. 2(a), the majority of the Ni-Ti powders exhibited spherical or near-spherical shapes, with smooth surfaces. The particle size distribution of Ni-Ti powder was assessed using a Mastersizer-3000 laser particle size analyzer (Malvern, England). The

Ni-Ti particles, which ranged in size from 26.2 μm to 64.3 μm, had an average size of 41.7 μm, as shown in Fig. 2(b).

The ultra-light Ni-Ti TPMS lattice structures were manufactured through a commercial DiMetal-100H laser powder-bed fusion (LPBF) machine (Guangzhou Laseradd Additive Technology Co., Ltd., Guangzhou, China) equipped with a 500-W ytterbium fiber laser. A near-equiatomic Ni-Ti substrate was subjected to preheating prior to the printing process. The printing process was conducted in a high-purity argon atmosphere, which resulted in the oxygen content within the build chamber being maintained blow 300 ppm. Based on the results and discussions of the orthogonal experiment in section 3.1, the selected LPBF parameters are presented in Table 1. The completed ultra-light Ni-Ti TPMS samples were removed from the substrate using a Mo filament cutter and were cleaned with absolute ethyl alcohol for a duration of 15 minutes, using an ultrasonic cleaner.

Table 1

L-PBF parameters

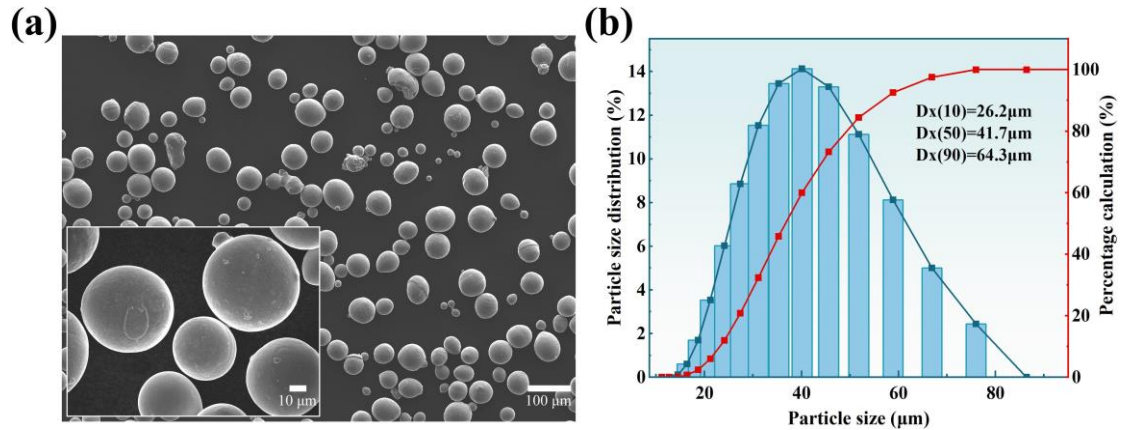| Laser power (w)	scanning velocity (mm/s)	layer thickness (μm)	hatch spacing (μm)	Hatch angle (°)	volumetric energy density (J/mm^3)
220	1400	40	70	90	56.12

Fig. 2. (a) SEM images of Ni-Ti particles and (b) particle size distribution of Ni-Ti powders.

2.3 Measurement and characterization

The relative density of the ultra-light Gyroid lattice samples fabricated by LPBF was defined as the ratio of their actual density to the theoretical density, which is 6.45 g/cm^3. The actual densities of the printed samples were determined using the Archimedes method, employing a ME204 electronic balance (METTLER, TOLED, Swizerland), which has a smallest scale increment of 0.1 mg. The percentage deviation in volume fraction between the Ni-Ti TPMS lattice structures fabricated by LPBF and designed CAD model was calculated as the ratio of the difference between the actual and designed volume fractions to the designed volume fraction. The actual volume fractions of the LPBF fabricated specimens were obtained by dividing the actual volume of as-built lattice to the total volume of the cubic sample. The actual volume of as-built samples was measured via the Archimedes method. The corresponding volume of the cubic samples was calculated after their overall dimensions were measured using a digital Vernier (Greener, China), which has a minimum scale division of 0.01 mm. In the orthogonal experiment, a Vtomex micro focus x-ray computed tomography (micro-CT) (General Electric Company, Germany) was utilized to scan and reconstruct the Ni-Ti Gyroid lattice samples manufactured by LPBF. The micro-CT reconstructed models were overlaid on their original CAD models for comparison using the VF Studio MAX 2.2 software (Volume Graphics, Germany). This allowed for further analysis of the struct diameter and surface deviations between the actual and designed lattice.

The compressive mechanical behaviors of ultra-light Ni-Ti Gyroid TPMS lattice samples manufactured by LPBF were evaluated using an AG-IC high-temperature endurance testing machine for materials, capable of applying the maximum load of up to 100 kN load (Shimadzu, Japan). In preparation for the test, the bottom surface of the model was secured to the test bench, while its top surface was gently connected to the upper plate of the testing machine. According to ISO 13314:2011 [37], the uniaxial compression test was conducted at a strain of 2.4 mm/min (equivalent to a 0.1% strain rate of the entire lattice structure) along the build direction (Z-axis) under room temperature conditions. And, the test will conclude once the total deformation reaches 80% of the model's original height. The stress was determined by dividing the applied load by the initial cross-section area of the ultra-light Ni-Ti lattice structure, which is perpendicular to the build direction. On the other hand, the strain was computed by dividing the displacement of the upper compression plate by sample's original height. Simultaneously, the overall compression process of various ultra-light Ni-Ti Gyroid TPMS lattice structures was captured using a digital camera (Canon, Japan) throughout

7

the experiments. Data points such as yield strength, yield strain, Young's modulus, ultimate strength, and ultimate strain were exacted from the stress-strain curves.

During the superelastic performance evaluation of the ultra-light Gyroid TPMS lattice structures, we utilized an E45.105 electronic universal testing machine (MTS, America) to conduct cyclic compression tests on the lattice samples. The initial condition of the specimens is the same as that in the uniaxial compression test. However, to prevent premature fracture, the machine's upper plate oscillates up and down at a steady pace of 1.2 mm/min, which is 1/2000th of the model's height. Once the upper plate reached the predetermined value (8% strain of the entire lattice structure, equivalent to 3.2 mm), it would cease its downward movement and begin unloading. Subsequently, the plate returned to its initial position and initiated another compression cycle, identical to the first. This superelastic experiment was conducted over a total of 15 cycles. The computer continuously recorded the relationship between the displacement and load of the top plate. Data such as recoverable strain, irrecoverable strain, and recoverable rate were exacted from the cyclic compression stress-strain curves.

We employed a TA-DSC2500 differential scanning calorimeter (DSC) (TA, America) to identify the characteristic temperatures with the martensitic transformation. Prior to the DSC test, the lattice specimen was polished with sandpaper to remove the oxide layer from the lattice structure. The samples were first heated from -80 ℃ to 100 ℃, then cooled from 100 ℃ to -80 ℃, maintaining a consistent heating and cooling rate of 10 ℃/min. The start and finish temperatures for the forward martensitic transformation (M_s and M_f), and the start and finish temperatures for the reverse martensitic transformation (A_s and A_f), were determined from the DSC curves through a tangent method. The SME responses of ultra-light Ni-Ti Gyroid lattice structures were assessed through a series of dual cyclic loading-unloading-heating experiments. Specifically, we utilized the E45.105 electronic universal testing machine to conduct a cyclic loading-unloading-heating experiment. The initial condition of the samples was identical to that of the superelastic experiment, including the testing machine's speed. Compared with the superelastic experiment, during the cyclic loading-unloading-heating experiment, the testing machine would pause once its upper plate returned to the initial position. Subsequently, the specimen was immersed hot water at 80 ℃ (a temperature higher than A_f temperature) for 3 minutes to ensure the complete transformation of the detwinned Martensite into Austenite. Subsequently, the sample was returned to the bottom plate of the testing machine, with the initial condition being

the same as before. The process of loading, unloading, and heating was considered a cycle. This experiment was conducted over a total of 2 cycles. However, it is worth noting that, to determine the sample's height after the second heating, it would be returned to the bottom plate of the testing machine after the second heating, followed by the testing machine carrying out another loading-unloading cycle.

2.4 Finite element method

FE method was utilized to examine the stress distribution on the surface of the ultra-light Gyroid TPMS lattice structures under compressive loading. The analysis was conducted using ABAQUS 2020. The 3D solid element, specifically of the 4-node tetrahedral type was used to create a mesh for the ultra-light lattice models in the simulation processes, with each node having six degrees of freedom. To balance simulation efficiency and the required accuracy, an element size of 0.25 mm was selected. The minimum time increment size was established at 1×10^{-6} s and an isotropic plastic hardening model with an initial strength of 508 MPa was chosen[38]. In all simulations, the Ni-Ti material was presumed to have an elastic modulus of 57.0669 GPa, with a Poisson's ratio of 0.34. The Johnson-Cook (J-C) damage model was employed to assess the failure deformation and fracture behavior of ultra-light lattice structures. The values of J-C damage constants were determined based on the previous work [3].

3. Results and discussions

3.1 orthogonal experiment

On the one hand. according to the expression of Energy density, $E = P / (v \times h \times t)$, in which P, v, h, and t denotes laser power, scanning speed, hatching space and layer thickness, respectively. As mentioned in section 2.2, the average size of Ni-Ti particles was 41.7 μm, which led to the selection of a laser thickness value of 40 μm [39]. Furthermore, based on prior studies, the hatching space was selected at 70 μm. The additional printing parameters, P and v, were determined via an orthogonal experiment, with the parameter combinations outlined in Table 2. The model designed for the orthogonal experiment was a Gyroid lattice structure measuring 20 mm × 20 mm × 20 mm, with a unit cell size of 10 mm and a volume fraction of 4%. The detailed methodology for the design was elaborated upon in section 2.1. As depicted in Fig. 3(a), all four sets of samples remained intact, with no signs of strut fractures or visible cracks. Upon examining the struts from A1 to A4 in set A from top view, they appeared brown,

and, in some cases, purple. This suggests that the energy density values for Set A were excessively high, leading to an overburning effect. In comparison, set B exhibited a less pronounced   overburning appearance, while set C and set D showed almost no signs of overburnig. Based on the energy density values of sets C and D, an energy density range of 33.1 to 78.6 J/mm^3 was deemed more suitable. In addition, as presented in Fig 3(b), there was a decrease in actual volume fraction of samples as the scanning speed increase, give a constant laser power. With a fixed scanning speed, the volume fraction of samples exhibited an upward trend with the increase in laser power. <mark>In conclusion, energy density significantly influenced the volume fraction of samples produced by LPBF. An increase in the volume fraction of LPBF printed samples can be attributed to a higher energy density, which results from a decrease in scanning speed and an increase in laser power. This is because</mark>. The Fig. 3(c) illustrates the percentage deviations in volume fractions of the samples printed in the orthogonal experiment. With a constant scanning speed, the percentage deviations increased as the laser power escalated, a phenomenon consistent with that shown in Fig. 3(b). When the laser power remained unchanged, the percentage deviations increased with a decrease in scanning speed. This can be attributed to the fact that an increase in laser power and a decrease in scanning speed result in a higher energy density, ultimately leading to an increase in the percentage deviation of volume fractions across the printed samples. Moreover, the presence of both positive and negative percentage deviations suggests there exists an optimal energy density that allows the actual VF of the samples to closely match the designed CAD model. Among these findings, the printing parameters with a percentage deviation of -1.2% were deem relatively reasonable.

Table. 2. Parameter combinations of orthogonal experiment for exploring printing parameters.

Set	Laser Power (W)	Scanning Speed (mm/s)	Energy Density (J/mm^3)	Relative Density (%)
A1	130	400	116.1	98.9%
A2	160	400	142.9	99.0%
A3	190	400	169.6	98.4%
A4	220	400	196.4	98.9%
B1	130	700	66.3	99.1%
B2	160	700	81.6	98.9%

B3	190	700	96.9	98.8%
B4	220	700	112.2	99.1%
C1	130	1000	46.4	99.1%
C2	160	1000	57.1	99.7%
C3	190	1000	67.9	98.0%
C4	220	1000	78.6	99.5%
D1	130	1400	33.2	98.3%
D2	160	1400	40.8	99.9%
D3	190	1400	48.5	98.7%
D4	220	1400	56.1	99.1%
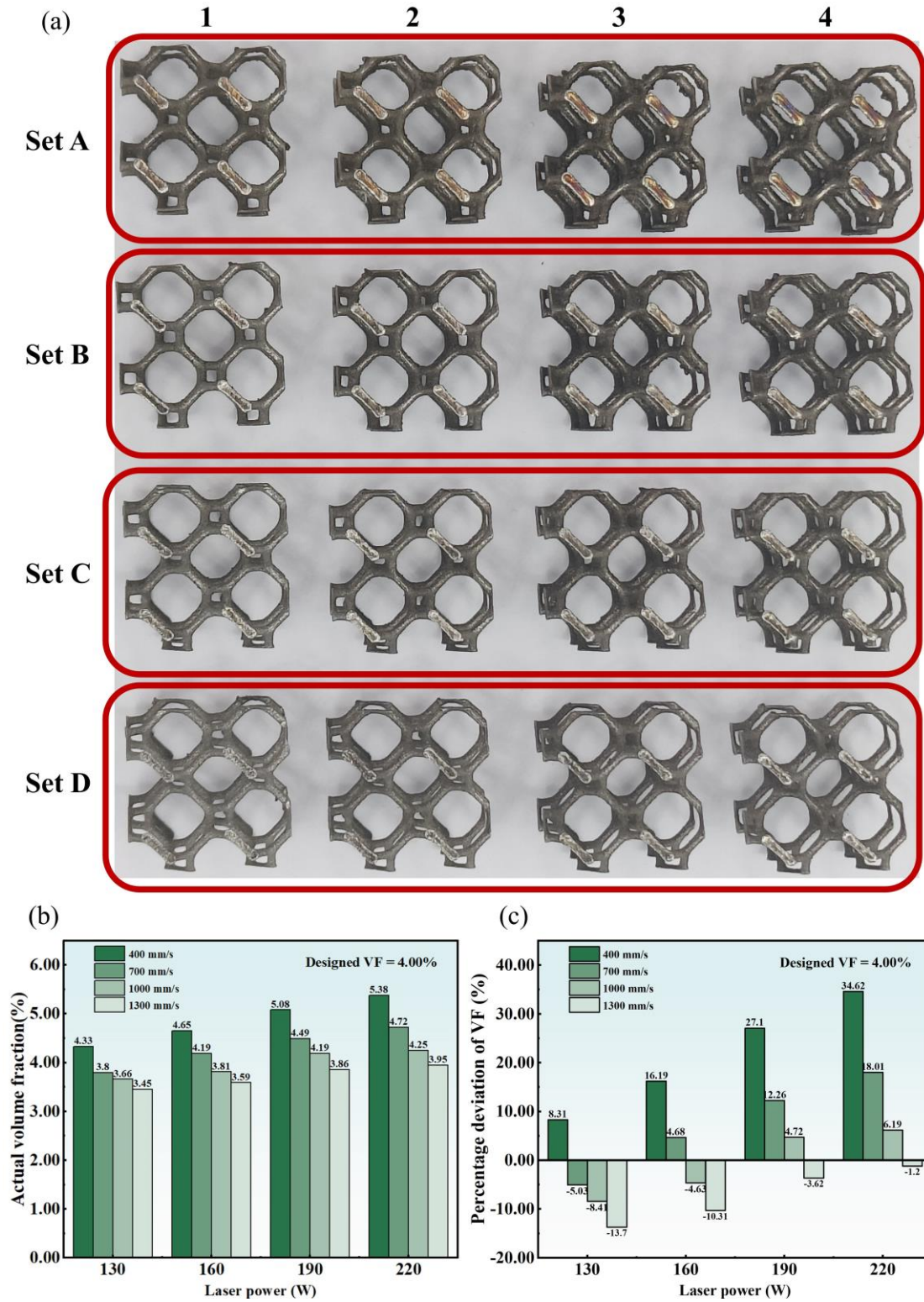
Fig. 3. (a–b) Images of L-PBF-fabricated Ni-Ti Gyroid TPMS lattice structures with different printing parameters; (c) Actual volume fraction of various fabricated samples; (d) Percentage deviations of volume fraction.

In addition, Fig. 4(a-b) showcases the surface deviation maps alongside SEM images of LPBF fabricated A4 and D4 samples. These were compared to the designed

12

CAD model, a comparison made possible through micro-CT analysis and SEM. Neither of the samples showed damaged struts or significant defects, yet their rough surfaces were clearly observed. This phenomenon was consistent with those made in Fig. 3(a). It is also worth noting that the most pronounced surface deviations were primarily observed at the upper inner walls of pores in both samples. However, the D4 sample, which has a lower energy density, exhibited far fewer surface deviations than the A4 sample. This is primarily because when the energy density is high, the melt pool expands, leading to more powder solidification in unsupported areas[38]. Moreover, the microscopic images in Fig. 4(a-b) reveal that the front view of LPBF fabricated samples were characterized by stair-stepping effect and tiny powder particles attached on the surfaces. It is evident that the size of powders adhering to the A4 sample was larger than that of D4 sample, indicating a suggesting lower fidelity when using relatively high energy density in the LPBF process. This observation aligns with the findings from the CT-reconstructed models. Furthermore, the surface deviation of the D4 sample in Fig. 4(c) followed a Gaussian distribution and ranges from -0.092 mm to 0.102 mm, with an average surface deviation of -0.0102 mm. This demonstrates excellent manufacturing accuracy of ultra-light Ni-Ti Gyroid lattice structures via D4 printing parameters. In contrast, the surface deviation of A4 sample in Fig. 4(c) was not of Gaussian distribution, as indicated by the smooth section highlighted by the red circle. This may be caused by relatively high energy density of A4 printing parameters leading to too much adhered powders generated. Also, the adhere powders were primarily clustered around the upper inner walls of pores, resulting in nearly identical surface areas within the 0.0 to 0.2 mm deviation range. Additionally, the trends in strut diameter for the A4 sample, D4 sample and CAD model were nearly identical, except for the sub-peaks appearing at a diameter lower than 0.42 mm for both the A4 sample and D4 sample, as indicated by blue rectangle as illustrated in Fig. 4(d). Notably, the limit of 0.42 mm was close to the average diameter of Ni-Ti powders used in this study, demonstrating that these sub-peaks perhaps could be attributed to the noise of the adhered powder particles [34]. It is worth noting that the sub-peak of D4 sample was far lower than its A4 counterpart, indicating that fewer adhered powder particles on the D4 sample and suggesting that its parameters for LPBF process were more appropriate. Significantly, since these sub-peaks are caused by adhered powder particles, the corresponding data will be excluded in the analysis of the average strut diameters for the both samples. As shown in Fig. 4(e), the average strut diameters of both samples were higher than that of CAD model, which can be attributed to the powders that

adhered during the LPBF process. Besides, it was observed that the average strut diameter of A4 sample was 0.09 mm greater than that of the D4 sample. In contrast, the diameter of the D4 sample was only 0.01 mm larger than that of CAD model. This indicates that the printing parameters associated with the D4 sample yield superior manufacturing accuracy.

In conclusion, the orthogonal experiment confirms that the D4 printing parameters yield the highest quality and precision in manufacturing. Consequently, all LPBF fabricated specimens in the following experiments are manufactured using D4 printing parameters.
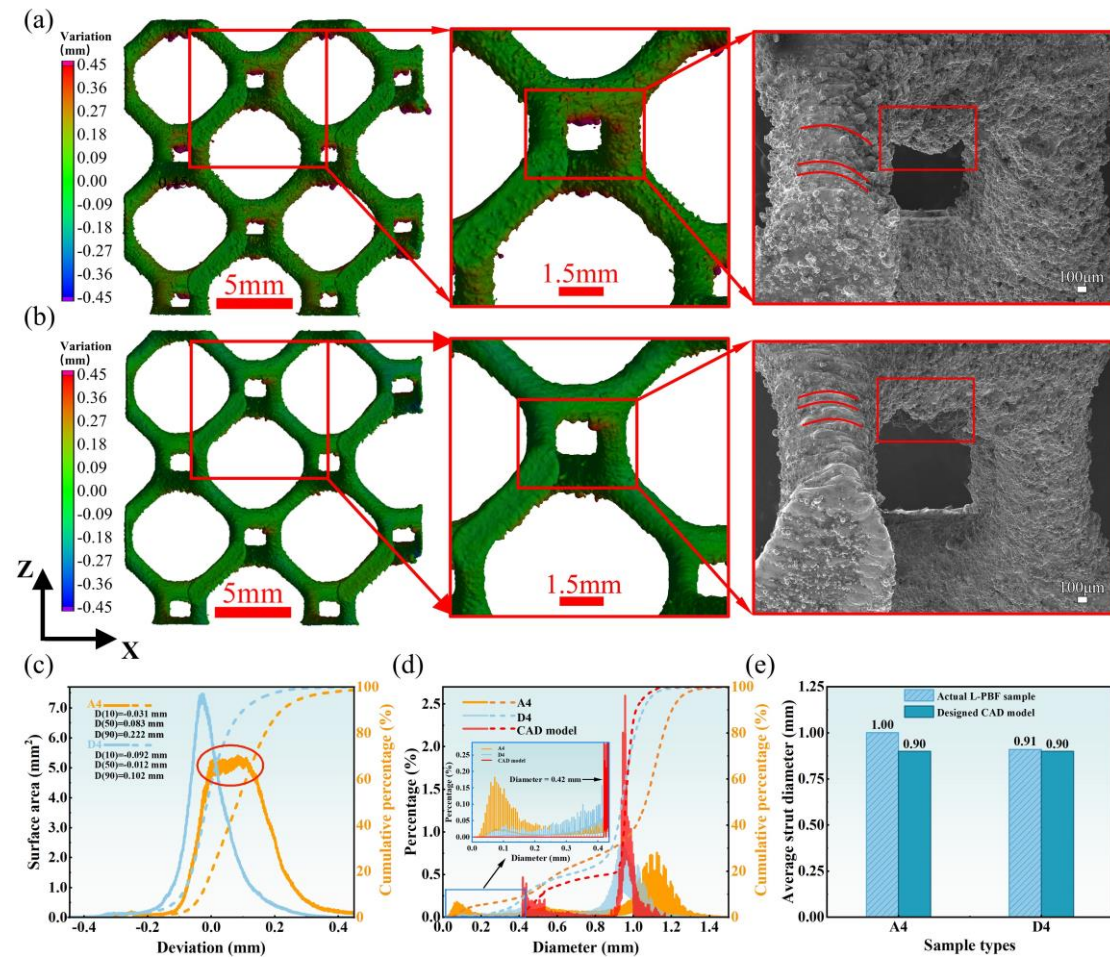
Fig. 4. Surface deviation maps and SEM images of (a) A4 and (b) D4 printed samples; (c) Statistical surface deviation distributions of A4 and D4 sample; (d) Statistical strut diameter distributions of fabricated samples and CAD model; (e) Average strut diameters of samples and CAD model.

3.2. Compressive responses and mechanical properties.

Fig. 5(a) presents the mechanical compression behavior of ultra-light Ni-Ti Gyroid specimens with varying volume fractions produced through LPBF. On the whole, the stress-strain curves of different samples with identical structures were comparable, indicating that LPBF process can consistently reproduce the Ni-Ti lattice structures. Moreover, despite the diverse mechanical properties of samples with different VFs, the lattices demonstrated similar mechanical responses across four stages.

The first stage is characterized by typical elastic deformation, during which the compressive stress rises linearly in response to increasing strain. In this phase, the slope of the curve represents the compressive Young's modulus of the model. The subsequent stage, referred to as the elastic-plastic stage, is marked by the stress-strain curve starting to deviate from the linear response. Additionally, during this stage, the stress point at which the stress-strain curve for uniaxial compressive loading deviates from the linear-elastic region by a strain of 0.2% is defined as the nominal yield strength and the corresponding strain is identified as the yield strain. Moreover, the stress during this stage escalates nonlinearly as the increase in strain until it attains the peak stress that the specimen can withstand. This is referred to as the ultimate strength, and the corresponding strain is termed as the ultimate strain. Upon surpassing the ultimate strength and the brief yield plateau, the stress begins to decrease significantly. Subsequently, the stress-strain curve enters the third stage, a prolonged plateau region characterized by fluctuating stresses, which contracts with the stable long plateau period of the uniform TPMS lattice structures investigated by Yang[40]. Finally, the majority of the struts in the lattice are severely damaged and compacted, leading the stress-strain curve into a densification stage, where the stress markedly escalates with the increasing strain.

The mechanical performance of the ultra-light Ni-Ti Gyroid TPMS lattice structures with various VFs is depicted in Figs. 5(b-f). The findings indicate an upward in the yield strength, Young's modulus and ultimate strength of the samples as the volume fraction increases. Specifically, the yield strength, Young's modulus and ultimate strength of the sample with the volume fraction of 1% were 0.063, 1.83 and 0.093 MPa, respectively, while the those of the specimen with a volume fraction of 4% were 0.954, 41.63 and 1.796 MPa, respectively. In addition, variations in yield strain and ultimate strain were observed. For example, the yield and ultimate strains of the sample with a volume fraction of 1% were 3.00% and 8.01%, respectively, while those of the specimen with a volume fraction of 4% decreased to 2.63% and increased to 14.70%, respectively. Notably, the smallest ultimate strain among 4 types of ultra-light

15

lattice structures is 8.01%, hence a compressive strain of 8.00% will be selected at 8.00% for cyclic compression in section 3.3.
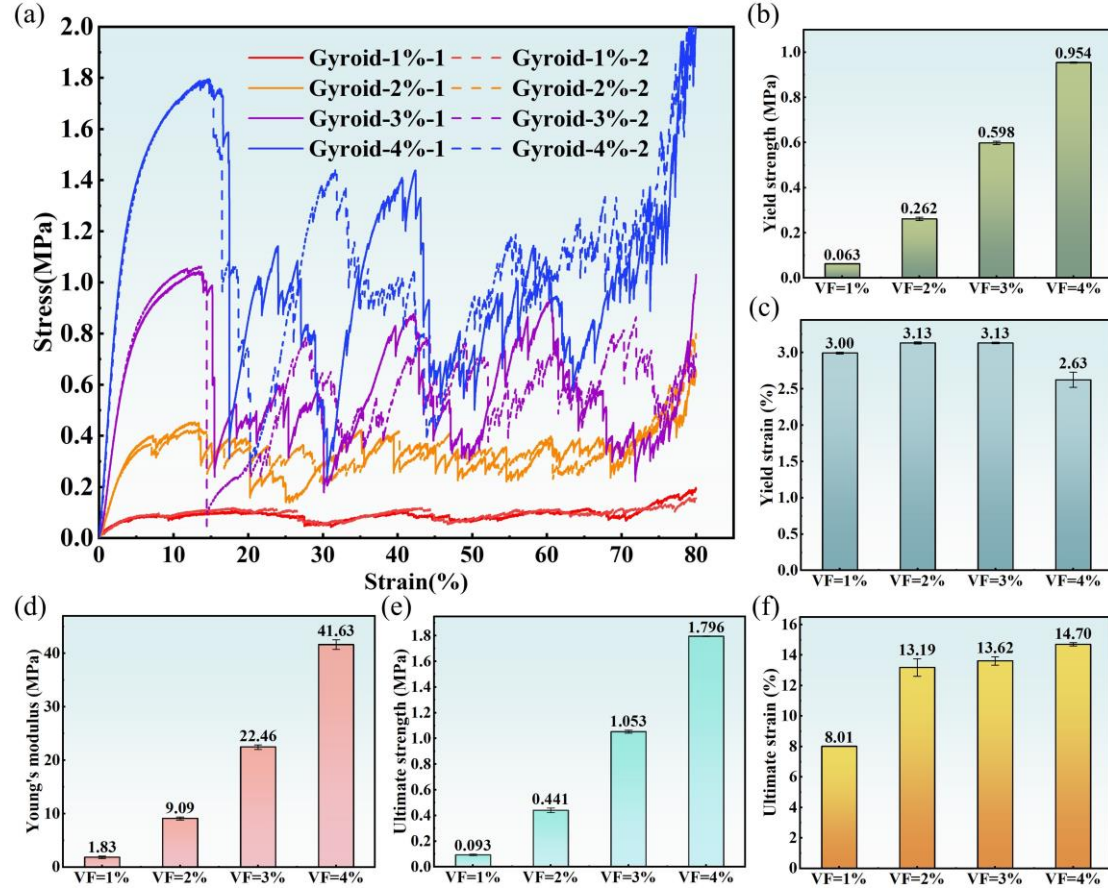

Fig. 5. Compressive mechanical responses at RT of Ni-Ti ultra-light Gyroid TPMS lattice structures with different volume fractions: (a) Uniaxial compressive stress-strain curves of the lattice structures; (b-f) Yield strength, yield strain, Young's modulus, ultimate strength and ultimate strain of several Gyroid lattice structures.

Fig. 6 showcases footages of ultra-light Ni-Ti Gyroid TPMS lattice structures with varying volume fractions, illustrating their progressions of deformation and collapse during uniaxial compression tests. In general, all lattice structures exhibited cracks when the strain reached 12%. However, for the samples with a volume fraction of 1% and 2%, the fractures occurred internally within the lattices, rendering the cracks unobservable on the ZoX plates. In contrast, for lattice structures with higher volume fraction such as 3% and 4%, minor cracks (indicated by red circles) were visible at the corners of the both lattice structures. Subsequently, all the samples exhibited a phenomenon of layer-by-layer collapse. It is worth noting that the initial collapse originated from the bottom layer, which can be attributed to the fact that the EDM process is unable to obtain smooth bottom surfaces for the samples.
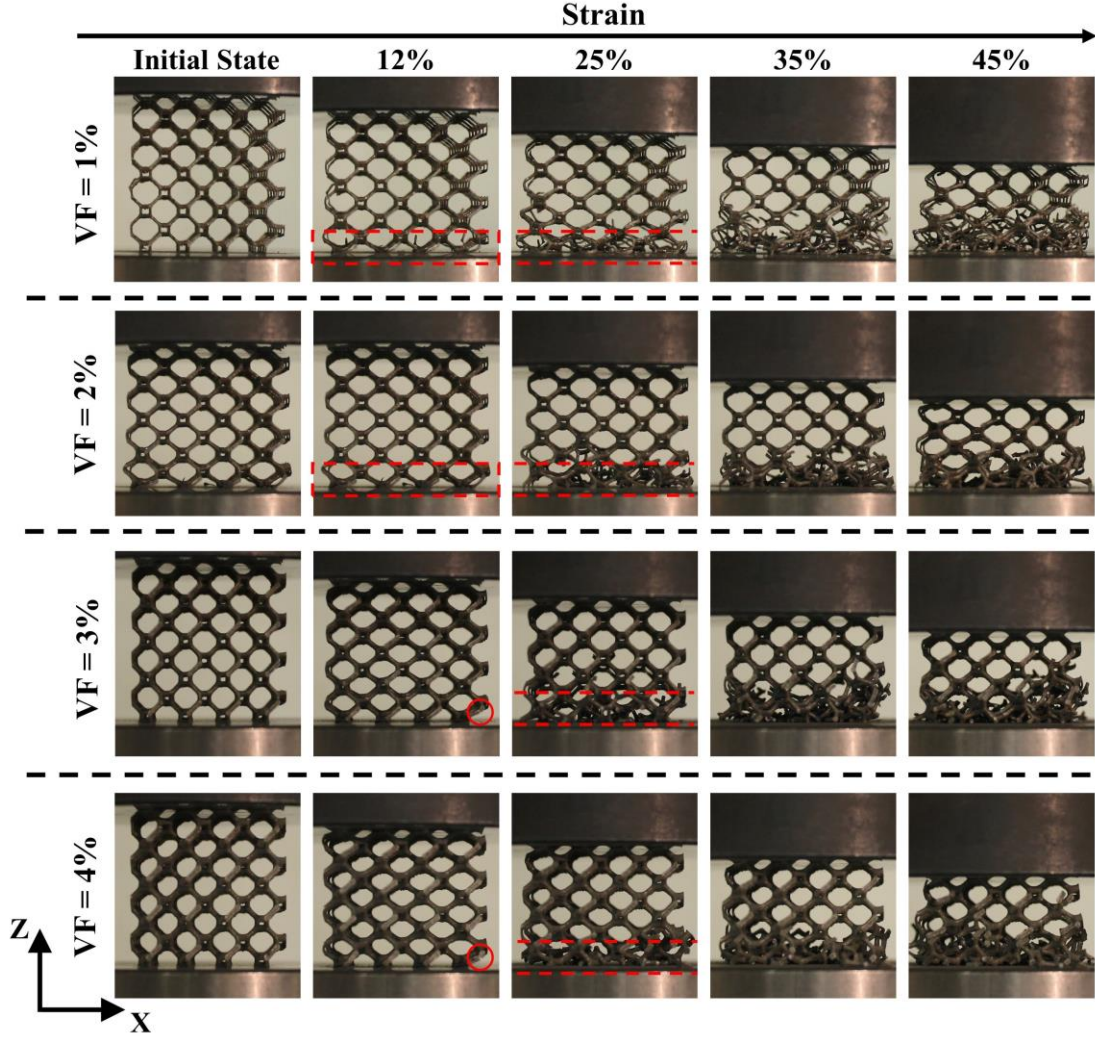
Fig. 6. Snapshots captured during uniaxial compression tests at diverse strain stages for ultra-light Ni-Ti Gyroid lattice structures with different volume fractions.

3.3. Cyclic compression and Superelasticity

Fig. 7 depicts the stress-strain curves for ultra-light Gyroid lattice structures across various volume fractions, subjected to 15 cycles of compression testing, with each cycle reaching a maximum strain of 8% and their mechanical behaviors. As shown in the Fig. 7(a-d), as the number of loading-unloading cycles increased, the stress-strain curves progressively shifted to the right, indicating a gradual rise and eventual stabilization of unrecovered strain. Furthermore, As shown in Fig. 7(e), the peak stress in the first cycles observed at the maximum strain of 8% escalated in tandem with the increasing volume fractions of the samples. Specifically, the lattice specimens exhibited maximum stresses of 0.0612 MPa, 0.2867 MPa, 0.5483MPa, and 0.9927 MPa at volume fractions of 1%, 2%, 3% and 4%, respectively. Additionally, following the initial cycles, the peak

stresses experienced minor fluctuations. This can be attributed to the minimal number of cycles inducing negligible mechanical damage to the structures. However, Fig. 7(e) reveals a significant variation in the Young's modulus across the samples. The values for specimens with VFs of 1%, 2%, 3%, and 4% increased from 1.576 MPa, 7.991 MPa, 15.373 MPa, and 31.983 MPa after the initial cycles to 1.766 MPa, 8.411 MPa, 18.975 MPa, and 39.282 MPa after the second cycles, respectively. In subsequent cycles, the Young's modulus exhibited slight fluctuations. This is probably due to the fact that the powders adhering to the specimens from the LPBF process were dislodged during the first loading-unloading compressive tests.
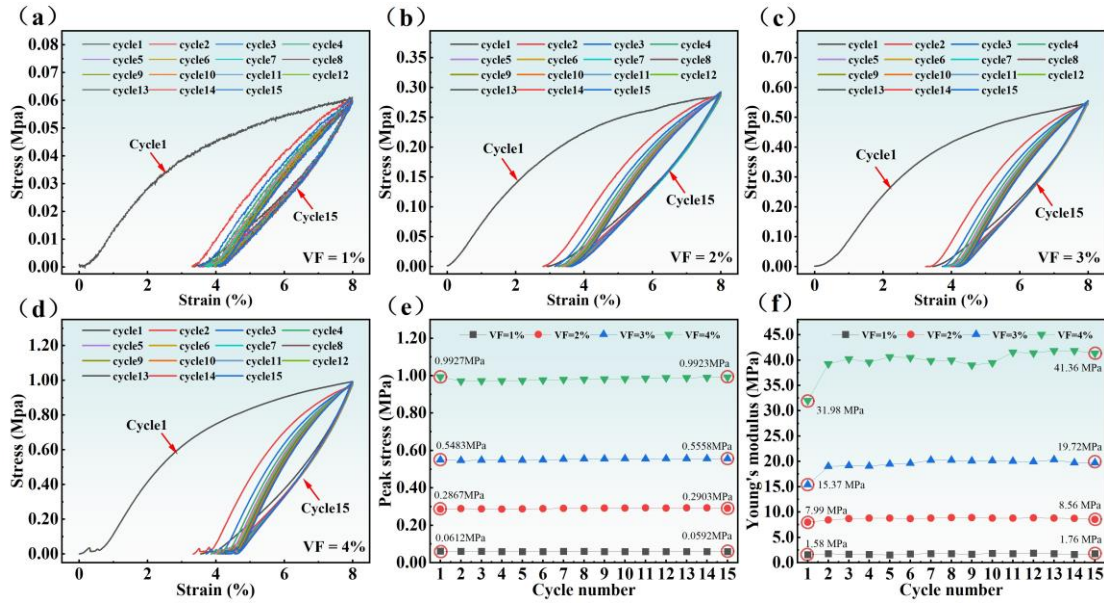

Fig. 7. Cyclic compression and mechanical behavior of various Ni-Ti ultra-light Gyroid lattice structures; (a-d) Cyclic compressive stress-strain curves of Ni-Ti ultra-light Gyroid lattice structures with various volume fractions; (e) Peak stresses of different cycles; (f) Young's modulus of various cycles;

Fig. 8 presents the analysis of the superelastic behavior across different structures. The residual strain (ε_{res}) is defined as the strain that remains after each loading-unloading cycle, while the recoverable strain (ε_{rec}) is defined as the difference between the maximum strain during loading and its corresponding residual strain in the same cycle. Fig. 8(a-b) depicts the ε_{res} and ε_{rec} across fifteen compression cycles. Notably, for the four ultra-light specimens, significant strains of 3.34%, 2.91%, 3.75%, and 3.55% respectively were observed. And, in the initial five cycles, the ε_{res} of all specimens exhibited a gradual increase, followed by a period of fluctuation in the subsequent ten cycles. Conversely, as shown in Fig. 8(b), their ε_{rec} exhibited an opposing trend, with a decrease observed in the first 5 cycles and then fluctuating in the final 10 cycles. This

The recoverable rates for the four ultra-light Gyroid TPMS lattice structures were computed using data from Fig. 7(a-d), and the results are presented in Fig. 8(c-f). It's worth noting that the logic depicted in Fig. 8(c-f) deviates from previous analysis shown in Fig. 8 (a-b). In this context, the recoverable rate is defined as the ratio of the recoverable strain to the total compressive strain for each cycle. Fig. 8(c) illustrates that the minimum recoverable strains for these lattice structures were all observed during the initial loading-unloading compressive cycle, ranging from 53.13% to 63.63%. In the second cycle, the recoverability percentage experienced a significant increase, ranging from 86.72% to 95.32%. Ultimately, during the subsequent cycles, the recoverable rates reached a state of stability at relatively high percentages. Furthermore, the average recoverable rates for the final 14 cycles of the lattice structures were computed, and a comparison was made with those from the initial cycles, as depicted in Fig. 8(d). The plot clearly illustrates that the recoverable rates of all lattice structures, were significantly higher than those observed in the initial cycles. Specifically, the differences for the lattice structures with VFs of 1%, 2%, 3% and 4% were 39.63%, 34.4%, 43.46% and 41.37%, respectively. Additionally, as depicted in Fig. 8(e), the unrecoverable strains after the first circles and the fifteenth circles were calculated, with the results presented in Fig. 7(e). It was observed that the unrecoverable strains in the initial cycles for all lattice structures, regardless of their VFs, were considerably higher than their counterparts. To be specific, the unrecovered strains after the first circles for the ultra-light lattices were all above 2.90%, while those after the fifteenth circles approached 0.00%. Indeed, after the first cycle, which was characterized by relatively high compressive strain, powders and oxides adhering to the surfaces of the ultra-light lattice structures were dislodged. Consequently, the recoverable rates could see a subsequential increase after the initial cycles and the unrecoverable strain significantly decreased.
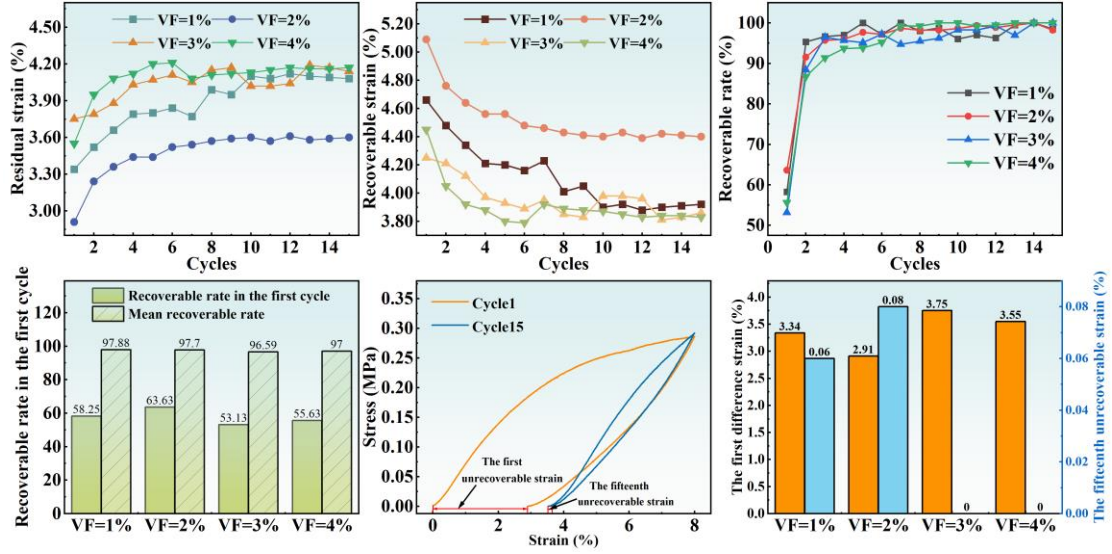
Fig. 8. The superelastic behavior of the four ultra-light Gyroid samples: (a) residual strains in each cycle; (b) recoverable strains in each cycle; (c) recoverable rate across different cycles; (e) recoverable rate in the first cycle and mean recoverable rate; (e) schematic of the calculation of unrecoverable rate; (f) the first unrecoverable strain and the fifteenth counterpart.

3.4. Shape memory effects

The DSC curve can display an endothermic peak during the transition from the martensitic to austenitic phases, indicating the recovery temperature and the manifestation of the shape memory effect [42]. Fig. 9 illustrates the temperature transformations of for both the Ni-Ti powder and printed sample. As shown in Fig. 9(a ~ b), the cooling and heating trends for cooling in both plots were strikingly similar despite the disparities in M_s, M_f, M_p, A_s, A_f, A_p temperatures after laser powder bed fusion process. This suggests that the selected printing parameters for the LPBF process were appropriate. The phase transformation temperatures were extracted and displayed in Fig. 9(c) and their corresponding differences，as shown in Fig. 9(d), the data for powder and specimen are closely aligned, and their differences, as shown in Fig. 9(d), are similar, with the exception of a greater variation between M_s and M_f for the specimen. This indicates that LPBF printed samples require a broader temperature range to transform from Austenitic phase to Martensitic phase during the cooling process.
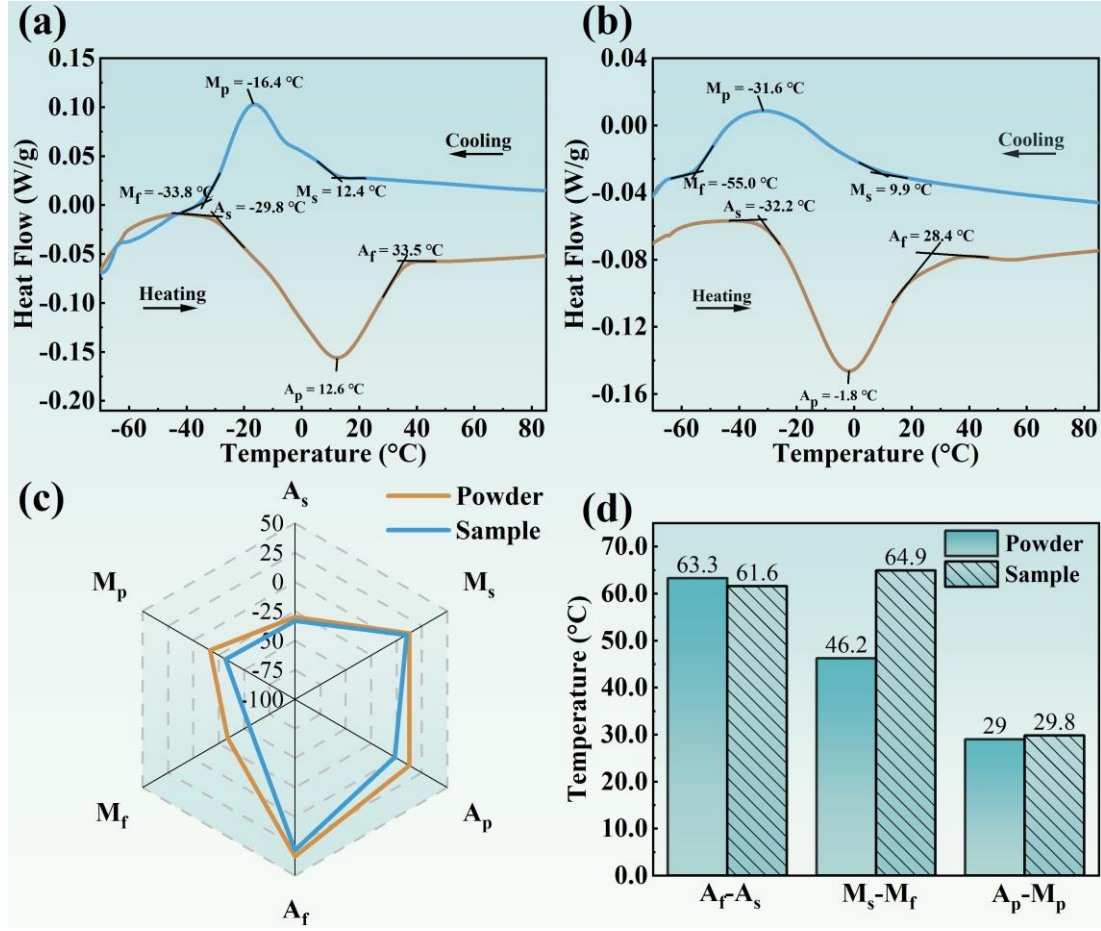
Fig. 9. Transformation of temperatures for Ni-Ti powder and printed sample; (a) DSC curve of Ni-Ti powder; (b) DSC curve of Ni-Ti Gyroid manufactured specimen.

Fig. 10(a-d) depicts the dual compressive loading-unloading-heating responses of ultra-light Ni-Ti Gyroid TPMS lattice structures with varying volume fractions (1%, 2%, 3% and 4%, respectively) at room temperature. Fig. 10(e) presents a schematic that outlines the methodology for analyzing the shape memory effect in this work. The corresponding data derived from Fig. 10(a-d) are displayed in Fig. 10(f - i).

According to Fig. 10(a-d), the lattices of varying VFs all experienced greater load during the initial circles compared to the subsequent ones. This phenomenon can be attributed to the inability of the lattices to revert to their original height following the initial heating, could not recover to its original height after the first heating, resulting in the lattice structures enduring less strain. Generally, as shown in Fig. 10(f)，the applied strain (ε_{tot}) for Ni-Ti alloys is composed of three distinct types of strain: elastic recoverable strain (ε_{e-rec}), recoverable strain after heating (ε_{h-rec}), and residual strain (ε_{res}). It can be seen clearly from the Fig. 10(f) that the total recoverable strain for all samples in the first cycle with VFs of 1%, 2%, 3%, and 4% was notably high (7.62%, 7.45%, 7.83%, and 7.92%, respectively). In contrast, their residual strains were

remarkably low (0.03%, 0.1%, 0.11%, and 0.08%, respectively). This suggests that ultra-light Ni-Ti Gyroid TPMS lattice structures exhibit excellent shape memory effects. Furthermore, the sample with a VF of 3% demonstrated the highest elastic recoverable strain and the lowest recoverable strain after heating in the first cycle among all samples. This implies that the Gyroid lattice structure with a VF of 3% exhibit superior superelasticity. On the other hand, the sample with a VF of 4% had the lowest elastic recoverable strain and the highest recoverable strain after heating among all samples, indicating that heating above the A_f temperature significantly impacts the Gyroid lattice structures with the VF of 4%. It is worth noting that in this study, even although the pre-set strain was 8%, the final applied strains were not all equivalent to 8% among all the samples. This is due to the fact that electric discharge wire cutting cannot guarantee precise dimensions for the cuttings. In the second loading-unloading-heating cycle, as depicted in Fig. 10(g), the trends for elastic recoverable strain, recoverable strain after heating and residual strain of all samples closely mirrored the corresponding data in Fig. 10(f). However, it was observed that the elastic recoverable strain of all samples in the second cycle were marginally lower than their corresponding statistics in the first cycle, a phenomenon that was consistent with the superelasticity test results presented in section 3.3. Conversely, their recoverable strain exhibited a slight increase and residual strain showed a gentle decrease in the first cycle, suggesting an enhanced shape memory effect in all the samples after the first cycle. As depicted in the Fig. 10(g), the total applied strains of all samples in the first cycle were consistently higher than those in the second cycle. This can be explained by the fact that after the first heating, all samples retained some residual strains. Specifically, the samples with VFs of 1%, 2%, 3%, and 4% had residual strains of 0.03%, 0.1%, 0.11%, and 0.08%, respectively.

The recoverable rate (δ_{rec}) serves as a crucial metric in the analysis for shape memory effect of Ni-Ti alloys. In this study, we compute the recoverable rate using the following formula:

$$\delta_{rec} = \frac{(\varepsilon_{e-rec} + \varepsilon_{h-rec})}{\varepsilon_{tot}} \qquad (3)$$

All pertinent data are presented in table. 2, and the calculated recoverable rates for various samples are depicted in Fig. 10(i). As can be observed from Fig. 10(i), in the first cycle, all samples demonstrated a significantly high recoverable rate, with the lowest value being 98.61%. This suggests that the ultra-light Ni-Ti Gyroid TPMS lattice structures exhibit a remarkable shape memory effect. Furthermore, in the second cycle, all specimens displayed a recovery percentage exceeding 99.36%, indicating that the shape memory effects of the ultra-light Ni-Ti Gyroid TPMS lattice structures maintain

a high level of stability even after initial loading-unloading-heating cycles. Finally, we calculate the average recoverable rate between the first and second cycles for comparison with other references in section 4.2.
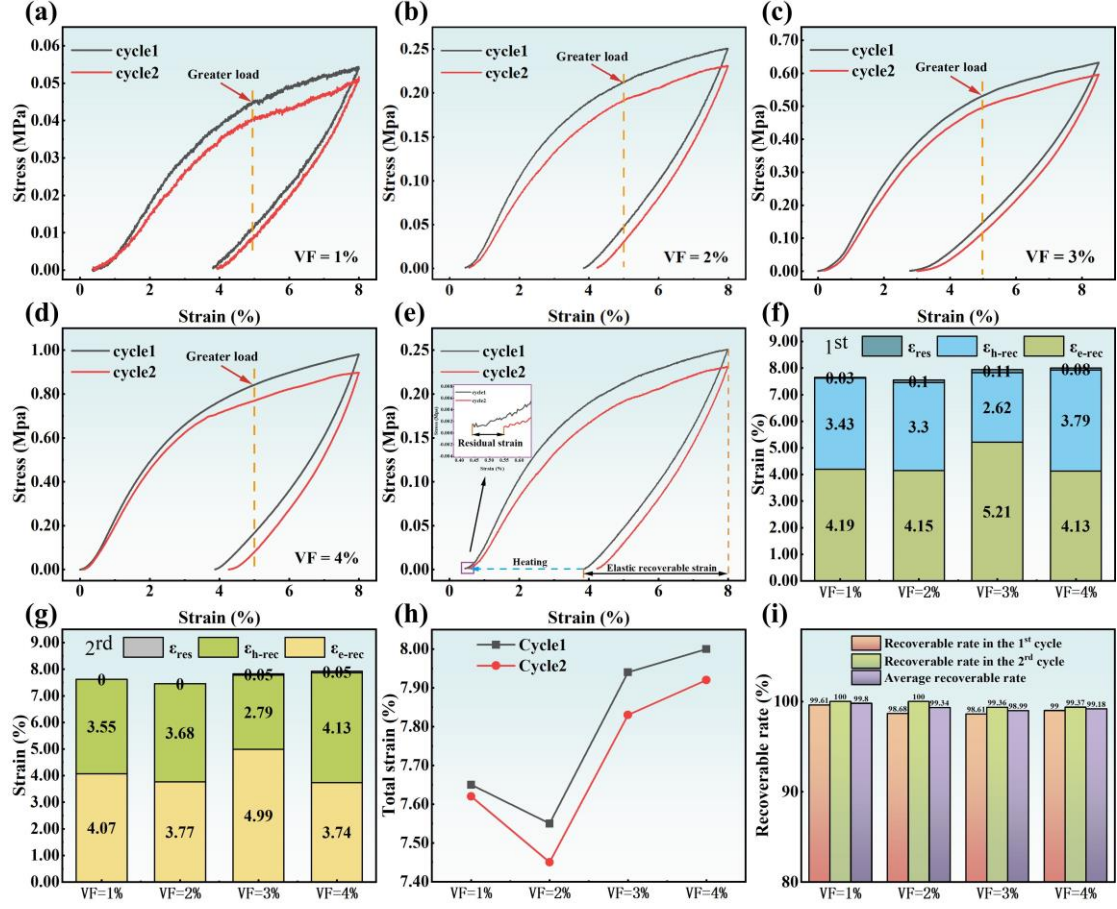

Fig. 10. (a-d) Double compressive loading-unloading-heating mechanical responses of Lattice structures owning diverse VFs of 1%, 2%, 3%, 4% at RT; (e) A schematic illustrating the analysis of the shape memory effect; (f-g) Residual strain, recoverable strain owing to heating, and elastic recoverable strain in the first cycle and second cycle; (h) Total applied strain for different structures during the first and second cycle; (i) Recovery rates for the ultra-light Gyroid TPMS samples.

Table. 2. Data of shape memory effect for the ultra-light samples.

VF(%)	The first cycle				The second cycle			
	$\varepsilon_{e\text{-}rec}(\%)$	$\varepsilon_{h\text{-}rec}(\%)$	$\varepsilon_{tot}(\%)$	$\delta_{rec}(\%)$	$\varepsilon_{e\text{-}rec}(\%)$	$\varepsilon_{h\text{-}rec}(\%)$	$\varepsilon_{tot}(\%)$	$\delta_{rec}(\%)$
1%	4.19	3.43	7.65	99.61	4.07	3.55	7.62	100.00
2%	4.15	3.30	7.55	98.68	3.77	3.68	7.45	100.00
3%	5.21	2.62	7.94	98.61	4.99	2.79	7.83	99.36
4%	4.13	3.79	8	99.00	3.74	4.13	7.91	99.37

4. Discussion

4.1 Finite element analysis

4.1.1 The stress concentration with different volume fractions

To comprehensively analyze the deformation behavior and stress distribution on the surfaces of Ni-Ti Gyroid lattice structures, a quarter-section of Gyroid lattice unit cell was extracted for further stress analysis, as depicted in Fig.11(a). Since the Gyroid lattice unit cell comprises four equivalent sub-layers[38], the quarter model can adequately represent the stress state of the entire Gyroid lattice structure. Fig. 11(b) demonstrates the force analysis and deformation of the quarter-section of Gyroid unit cell. Irrespective of the longitudinal elongation and torsion of struts, the overall deformation process for inclined struts AB and CD involves only lateral displacement and flexural rotation[43]. When subjected to compressive loading, the concave region experiences tensile stress due to tension, while the convex region undergoes compressive stress under compression as depicted by red and blue arrows, respectively.
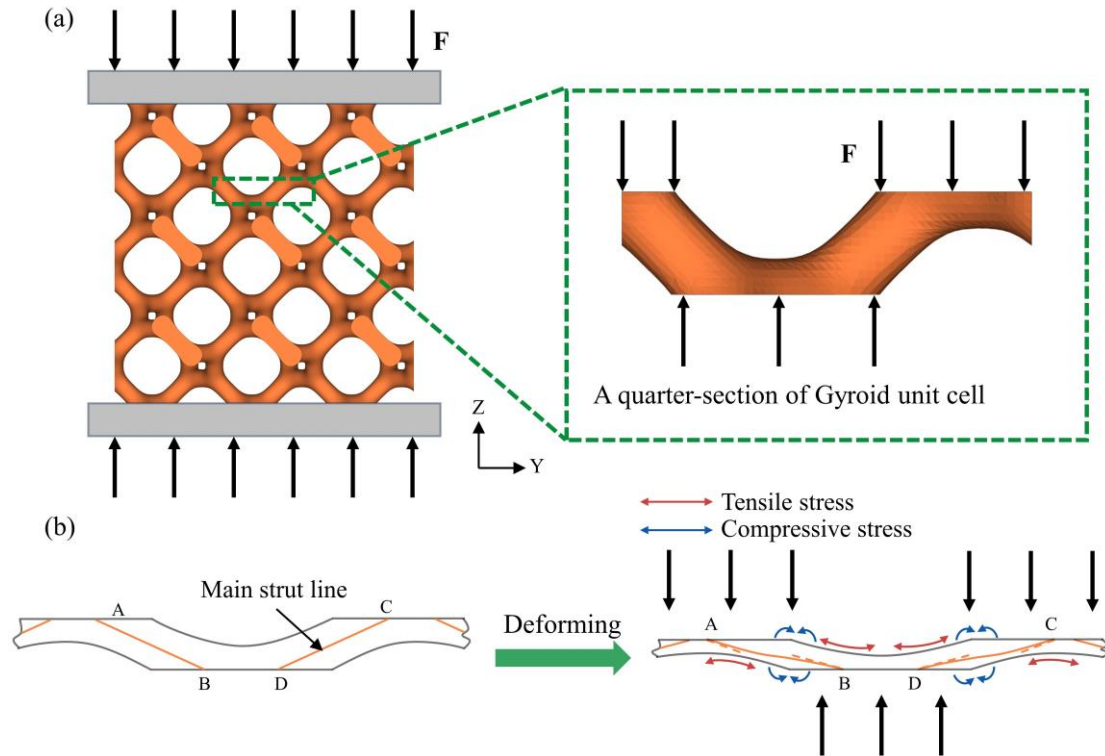

Fig. 11. (a) Schematic of extracting a quarter section of Gyroid unit cell; (b) deforming process under the compressive loading.

As depicted in Fig. 12, FE analysis of ultra-light Ni-Ti Gyroid lattice structures with VFs from 1% to 4% was also conducted to graphically illustrate the stress distribution. The figure illustrates the left views of maximum principal stress

distributions under monotonic compressive with 5% strain. It is clear that the stress for four lattice structures distributed uniformly above most of their surfaces and the distributions of tensile and compressive stress on the surface of the struts accord with the analysis illustrated in Fig. 11(b). In addition, the phenomenon that severe stress mainly exists in the lower surface of the inclined struts as indicated by round circles in Fig. 12.

To more effectively analyze the stress distribution for each ultra-light lattice structure, we determined the percentage of a specific stress range by calculating the ratio of the number of elements within this range to the total number of elements. Fig. 13 (a-d) depicts the frequency distribution of various stress ranges within the lattice structures. From these figures, it is evident that the general trend is a decrease in percentage as the stress level increases, regardless of the lattice structure's volume fraction. In this analysis, we defined the stress range of 0 to 133 MPa as the low-stress region, and any stress above 533.3 MPa as the high-stress region. The Fig.13 (e-f) display the frequency of low and high stress occurrences in various lattice structures, respectively. The volume fraction of the lattice structures likely plays a crucial role in determining their stress levels. For example, a structure with a volume fraction of just 1% exhibits an exceptionally high proportion (67.66%) of low stress and an exceedingly low frequency (0.80%) of high stress. Conversely, structures with volume fractions of 2%, 3% and 4% demonstrate comparable distributions of low and high stress.
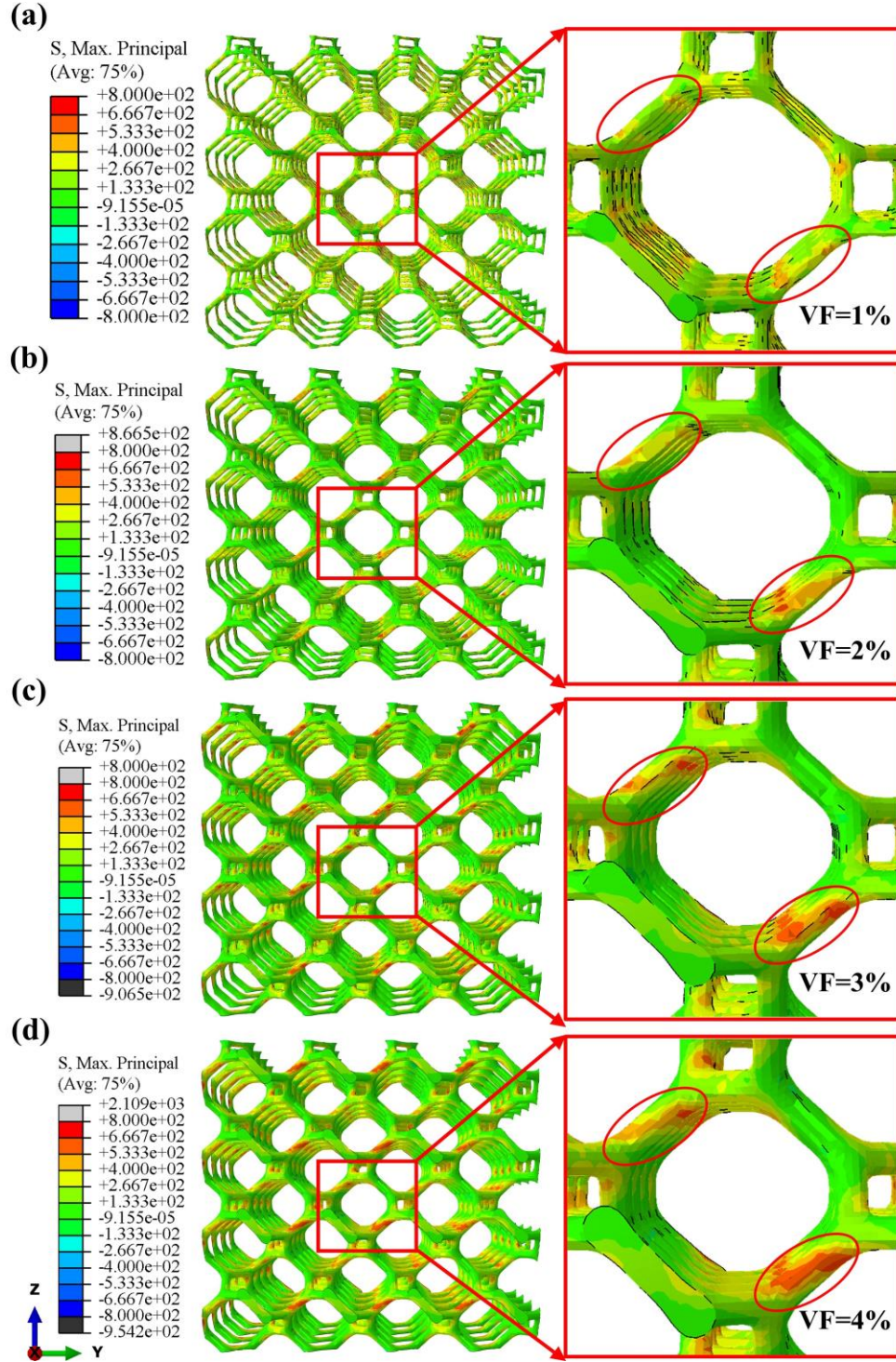
Fig.12. Stress distribution of ultra-light Gyroid lattice structures with volume fractions of (a)1%, (b)2%, (c)3% and (d)4%.
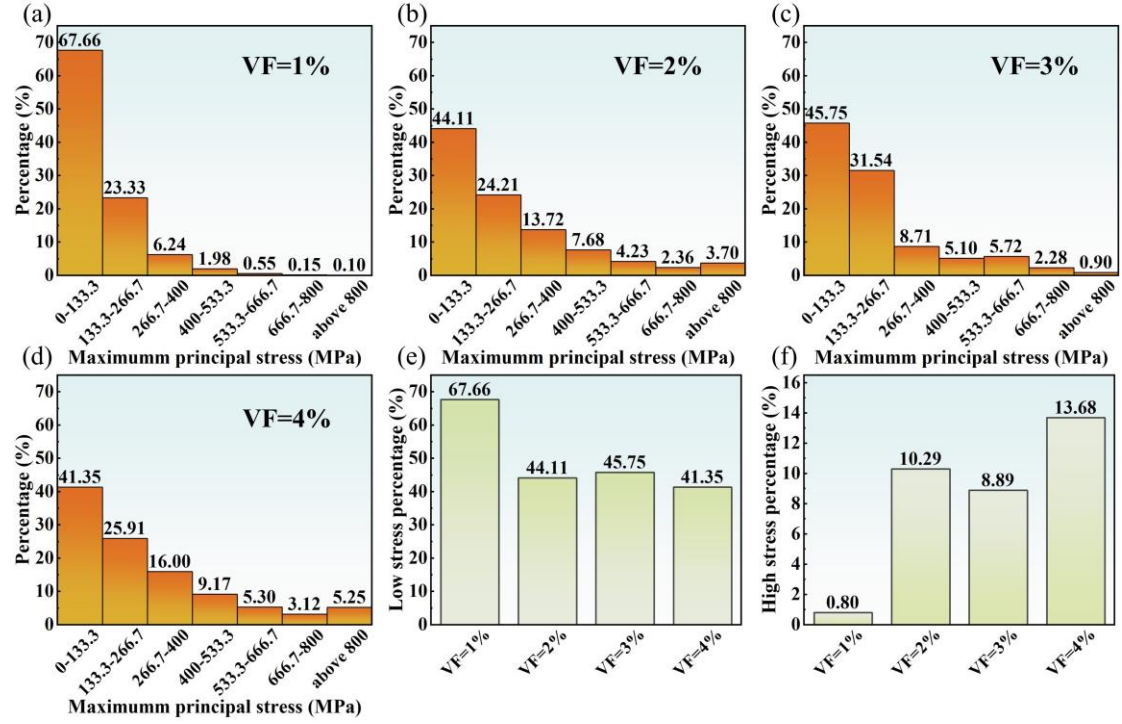
Fig.13. Histograms of each stress range of lattice structures with volume fractions of (a)1%, (b)2%, (c)3% and (d)4% as well as the frequency of (e) low stress and (f) high stress.

4.1.2 Deformation in finite element analysis

To gain deeper insights into the deformation mechanics of ultra-light Gyroid lattice structures, we conducted a simulation of a uniaxial compressive test. Notably, the compressive strain was intentionally limited to 45% in the finite element analysis. Fig. 14 illustrates the finite element analysis (FEA) of equivalent stress distribution and deformation performance of the lattice structures with varying volume fractions. Observations indicate that the onset of cracking in these structures typically began at approximately 13.5% strain. This deviates from the experimental findings where cracking occurred at around 12% strain as shown in Fig. 6. Notably, the locations of the cracks observed in the FE results mirrored those in the experimental data, predominantly appearing at the inclined struts. These results are consistent with the analysis presented in section 4.1.1. The analysis of equivalent stress distributions revealed that the stress is evenly distributed across these structures. Consequently, fractures are prone to occur at the top layer, as seen in the FEA of structures with a volume fraction of 2% and 4%, or at the bottom layer, as in those with a VF of 1% and 3%. In addition, for each structure, the simulation results reveals a layer-by-layer

compaction mode until it collapses into a densification mode [44], a phenomenon that mirrors the observations from the experimental data.
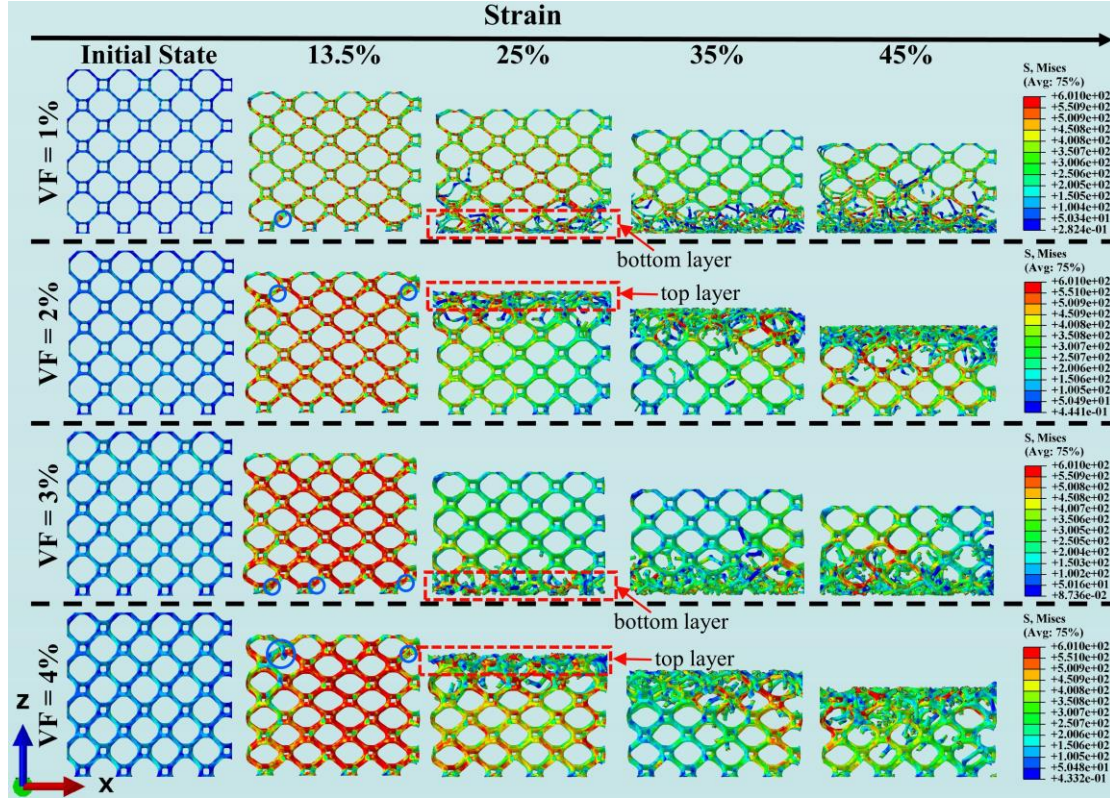

Fig.14. The FE results about the equivalent stress distribution and deformation behavior for ultra-light Ni-Ti Gyroid lattice structures with various volume fractions.

The comparison of compressive mechanical behavior between the experimental findings and FE results is presented in Fig. 15 to reveal the impact of manufacturing process on the Ni-Ti lattice structures characterized by their minimal volume fractions. Despite some discrepancies between the finite element simulation outcomes and the compressive tests as shown in Fig. 15. (a)-(d), the trends depicted in the stress-strain curves from the FE analysis align well with the experimental findings. The consistency of these trends substantiates the validity of the parameters employed in the FE method. However, it is notable that vast disparities of the mechanical properties extracted from the FE analysis and experimental data existed. Specifically, the Young's modulus of various structures derived from the FE analysis consistently exceed those obtained from experimental testing, albeit with minor variations. When it comes to the yield strength yield strain, and ultimate strength, the outcomes extracted from FE statistics are all far higher than those extracted from experimental data. Regarding the ultimate strain, the data from FEA and experimental tests are closely aligned, with the exception of a 6.54% strain discrepancy in structures that have a volume fraction of 1%. This deviation may

be attributed to a significant reduction in mechanical properties when the volume fraction falls below 2%, or potentially to inadvertent sampling processes that result in premature fracturing of some struts. Furthermore, in general, the discrepancies might seem substantial, yet considering the structures' low volume fractions, even slight imperfections such as porosities, cracks, holes, and the adhesion of partially melted powders-which are likely to occur during the LPBF process-can drastically reduce their mechanical properties. Consequently, for ultra-light Gyroid lattice structures, it is essential to employ post-treatment techniques to mitigate the impact of the LPBF process.
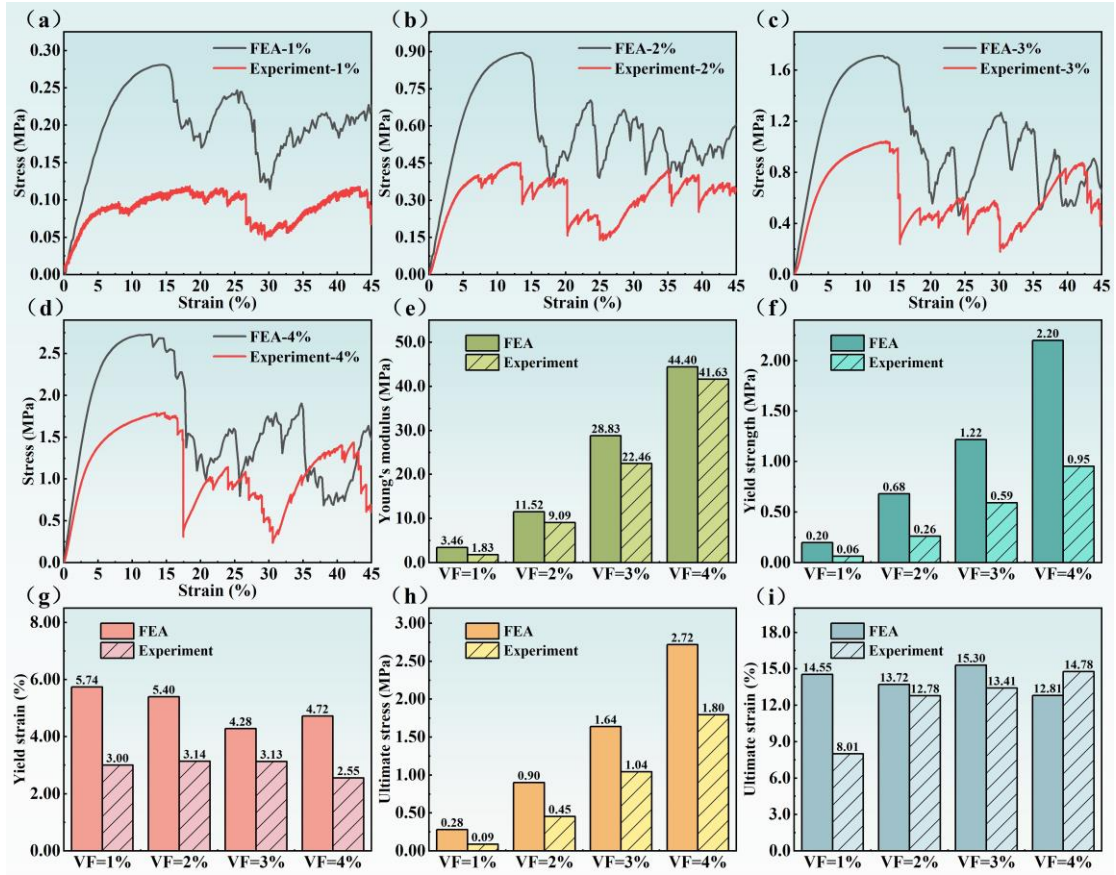

Fig.15. Comparative analysis of compressive mechanical properties: experimental vs. finite element (FE) results for ultra-light Ni-Ti lattice structures. (a)-(d) Compressive stress-strain curves for the lattice structures. (e)-(i) Evaluation of Young's modulus, yield strength, yield strain, ultimate strength and ultimate strain across various lattice configurations.

4.2 Comparison with other structures

Most studies investigating the superelasticity of NiTi structures employ ten cyclic loading-unloading tests, with authors typically presenting the initial and final data of

recoverable strain. Therefore, in this context, we focus on the recoverable rate at the tenth cycle. Importantly, as noted in section 3.3, the recoverable strain stabilizes after the initial cycles. Consequently, we define the tenth recoverable rate as the ratio of recoverable strain after the first loading-unloading cycle to the recoverable strain after the tenth cycle. Table. 3 illustrates the recoverable rates of the samples from this study for the convenience of comparison with other researches. Notably, in this work, the sample with a VF of 3% exhibits the highest recoverable percentage. This data point will be used for comparison with the maximum values reported in other studies.

Table. 3. Recoverable rate across various ultra-light lattice structures.

Volume fraction of different samples	Recoverable strain after the initial cycle (%)	Recoverable strain after the tenth cycle (%)	Recoverable rate (%)
1%	4.66	4.05	86.91
2%	4.40	5.09	79.56
3%	3.98	4.25	93.65
4%	3.87	4.45	89.97

Fig.16(a) provides a comparison of the superelastic properties across different NiTi structures. Previous studies reported recoverable rates ranging from 81.45% to 93.26% for normal porous structures, and 80.45% to 93.25% for solid structures. Notably, in our study, the sample with an ultra-light VF of 3% exhibited the highest recoverable rate of 93.65%. Therefore, it can be concluded that ultra-light NiTi Gyroid TPMS lattice structures possess relatively high superelastic properties.

As outlined in section 3.4, we used the average recovery rates from the first and second cycles of various sample to evaluate the shape memory effect, comparing these rates with those reported in other studies. It is important to note that the pre-set strains have a significant effect on the recovery rates of Ni-Ti shape memory alloys after heating. Specifically, lower pre-set strains result in higher recoverable rates [45]. In this study, the pre-set strains were 8%, while the pre-set strains in previous studies typically used a range of 2% to 8%. To more effectively assess the shape memory effect of the ultra-light Ni-Ti Gyroid lattice structures examined in this study, we compared our results with those from other studies that used pre-set strains ranging from 6% to 8%. As depicted in Fig. 16(b), previous studies reported recovery rates after heating that ranged from 90.38% to 96.5% for normal porous structures, and from 58.00% to 98.00% for solid structures. In contrast, our study found that the ultra-light Ni-Ti Gyroid lattice structures exhibited exceptionally high recovery rates, ranging from 98.99% to 99.80%. This finding underscores the remarkable shape memory effect of these structures.

Therefore, we can conclude that ultra-light Ni-Ti Gyroid TPMS lattice structures demonstrate outstanding shape memory effect properties.

Employing ultra-light Gyroid lattice designs to decrease the rigidity of the structure and counteract the irreversible martensitic phase transformation offers substantial benefits in boosting the superelasticity of NiTi structures. Considering that the majority of research is centered on the study of normal porous structures with VFs exceeding 5%, this work pioneers an exploration of ultra-light Gyroid lattice structures, offering valuable reference for fellow researchers. Moreover, the deployment of such structures shouble customized to fit particular scenaarios. For example, modifying the unit cell size of the ultra-light Gyroid lattice strutcures for us as implants in surgical procedures can help emulate the microsturcture of natural bone.

The design approach for ultra-light Gyroid lattice structures can also be applied to other TPMS lattice structures, including IWP and Primitive structures. Additionally, the TPMS_Scaffold_Generator [35] facilitates efficient acquisition of these ultra-light lattice structures, as illustrated in Fig. 17. In general, ultra-light TPMS lattice structures have significant versatility due to various TPMS styles and their distinctive geometries.
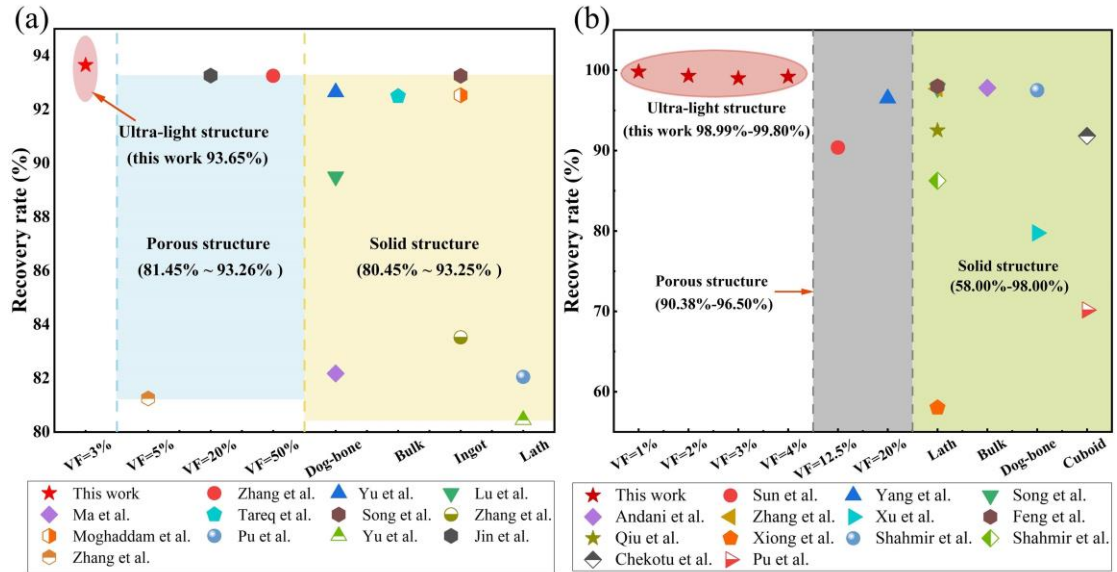

Fig.16. Comparison of (a) superelasticity and (b) shape memory effect of NiTi Gyroid lattice structures with other NiTi structures in the previous reports(文献已下载，但未引用，等待初稿返修确认).
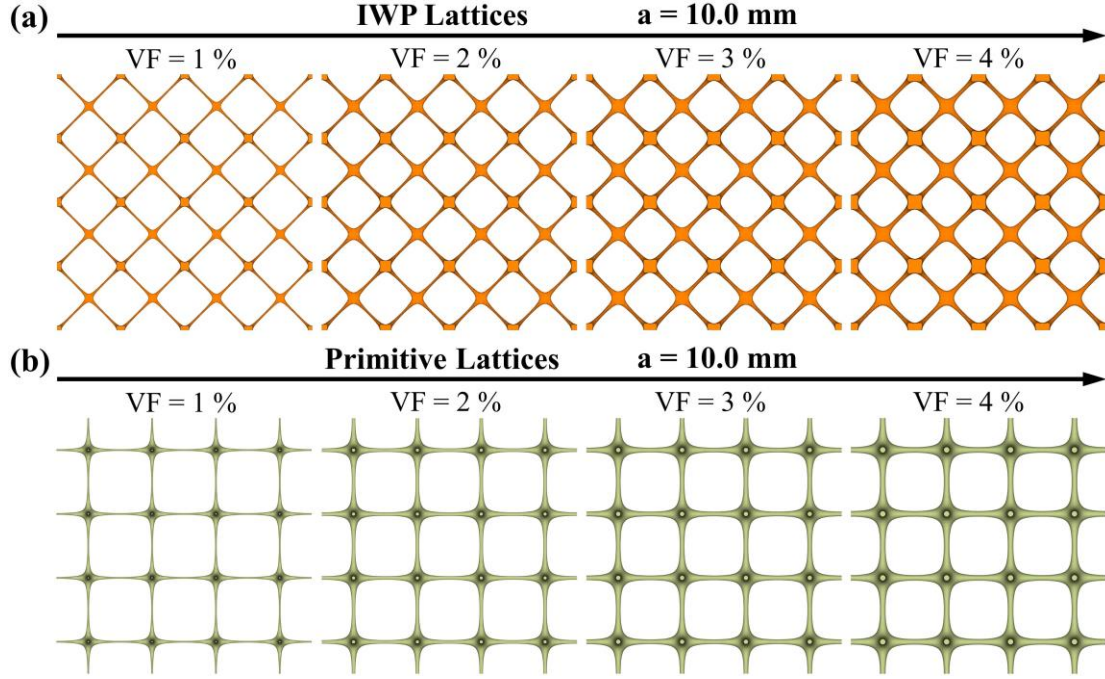
Fig. 17. Schematic diagram of ultra-light TPMS lattice structure design. (a) IWP lattice structures; (b) Primitive lattice structures.

5. **Conclusion** (需要查文献再作修改)

In this study, ultra-light Ni-Ti Gyroid TPMS lattice structures with various volume fractions (1%-4%) were designed, modeled, manufactured by LPBF. These structures were then characterized to determine the optimal printing parameters for the LPBF process, as well as to investigate compressive mechanical properties, superelastic behaviors, and shape memory effects of the ultra-light lattice structures. In addition, the stress distribution and fracture process of the lattice structure under load were analyzed using the finite element method. The major findings are as follows:

(1) For the orthogonal experiment, a Gyroid lattice structure measuring 20 mm × 20 mm × 20 mm, with a unit cell size of 10 mm, and a volume fraction of 4%, was designed and manufactured. The findings indicated that printing parameters with a higher energy density resulted in more adhered powders, which consequently led to lower manufacturing fidelity.

(2) A uniaxial compression test revealed that with an increase in volume fraction, there was a corresponding increase in the Young's modulus, yield strength, and ultimate strength of the structure, attributable to the increase in strut diameter. The finite analysis results demonstrated that the stress distribution of the structures was uniform during the deformation process. Furthermore, all the fractures occur on the inclined struts. The FE results of the deformation

processes and mechanical properties for the lattice structure were found to be in good agreement with the experimental results.

(3) Compared with other normal porous and solid structures reported in other works, the ultra-light Ni-Ti Gyroid TPMS lattice structures have superior superelasticity (recoverable rate of 93.65% for the Gyroid TPMS lattice structure with a VF of 4%). Moreover, the total shape recovery ratios of ultra-light Ni-Ti Gyroid TPMS lattice structures fabricated by LPBF were extremely high, ranging from 98.99% to 99.80%, indicating that an inspired shape memory effect for these ultra-light lattice structures.

CRediT authorship contribution statement

Di Lin: Methodology, Investigation, Data curation, Formal analysis, Writing-review & editing, Writing – original draft, Visualization. **Yunlong Ren:** Investigation, Methodology, Data curation, Conceptualization, Writing-review & editing. **Siqi Wu:** Methodology. **Mengying Chen:** Methodology. **Hui Qiao:** Methodology. **Lei Yang:** Methodology, Conceptualization, Data curation, Writing – review & editing, Code, Funding acquisition. All the authors read and approved the final manuscript.

Declaration of Competing Interest

The authors declare that they have no known competing financial interests or personal relationships that could have appeared to influence the work reported in this paper.

Acknowledgements

References:

[1] H. Zhang, M. Xing, W. Qian, S. Xing, J. Qiu, X. Liu, Defect engineering endows NiTi stents with photothermal-enhanced catalytic activity for high-efficiency tumor therapy, Journal of Materials Science & Technology 155 (2023) 227-237.

[2] G. Li, J. Bao, T. Yu, M. Chen, An atomistic study of effects of temperature and Ni element on the phase transition and wear behavior of NiTi shape memory alloy, Tribology International 192 (2024).

[3] J. Jin, S. Wu, L. Yang, C. Zhang, Y. Li, C. Cai, C. Yan, Y. Shi, Ni–Ti multicell interlacing Gyroid lattice structures with ultra-high hyperelastic response fabricated by laser powder bed fusion, International Journal of Machine Tools and Manufacture (2023).

[4] J. Pereiro-Barceló, J.L. Bonet, Ni-Ti SMA bars behaviour under compression, Construction and Building Materials 155 (2017) 348-362.

[5] M.R. Daymond, M.L. Young, J.D. Almer, D.C. Dunand, Strain and texture evolution during mechanical loading of a crack tip in martensitic shape-memory NiTi, Acta Materialia 55(11) (2007) 3929-3942.

[6] B. Ye, B.S. Majumdar, I. Dutta, Texture development and strain hysteresis in a NiTi shape-memory alloy during thermal cycling under load, Acta Materialia 57(8) (2009) 2403-2417.

[7] S. Dadbakhsh, B. Vrancken, J.P. Kruth, J. Luyten, J. Van Humbeeck, Texture and anisotropy in selective laser melting of NiTi alloy, Materials Science and Engineering: A 650 (2016) 225-232.

[8] K. Otsuka, T. Kakeshita, Science and Technology of Shape-Memory Alloys: New Developments, MRS Bulletin 27(2) (2002) 91-100.

[9] S. Barbarino, E.I. Saavedra Flores, R.M. Ajaj, I. Dayyani, M.I. Friswell, A review on shape memory alloys with applications to morphing aircraft, Smart Materials and Structures 23(6) (2014).

[10] S. Nemat-Nasser, W.-G. Guo, Superelastic and cyclic response of NiTi SMA at various strain rates and temperatures, Mechanics of materials 38(5-6) (2006) 463-474.

[11] S. Dadbakhsh, M. Speirs, J. Van Humbeeck, J.-P. Kruth, Laser additive manufacturing of bulk and porous shape-memory NiTi alloys: From processes to potential biomedical applications, MRS bulletin 41(10) (2016) 765-774.

[12] H. Vasudevan, V.K.N. Kottur, A.A. Raina, Proceedings of International Conference on Intelligent Manufacturing and Automation: ICIMA 2018, Springer2019.

[13] H. Zhang, B. Wu, S. Wang, Nitrogen-assisted laser-based powder bed fusion fabricated NiTi with high hardness and low modulus, Materials & Design 236 (2023).

[14] Y. Zhang, D. Wei, Y. Chen, L. Xie, L. Wang, L.-C. Zhang, W. Lu, G. Chen, Non-negligible role of gradient porous structure in superelasticity deterioration and improvement of NiTi shape memory alloys, Journal of Materials Science & Technology 186 (2024) 48-63.

[15] S.K. Sadrnezhaad, S.A. Hosseini, Fabrication of porous NiTi-shape memory alloy objects by partially hydrided titanium powder for biomedical applications, Materials & Design 30(10) (2009) 4483-4487.

[16] C.L. Chu, C.Y. Chung, P.H. Lin, Phase transformation behaviors in porous Ni-rich NiTi shape memory alloy fabricated by combustion synthesis, Materials Science and Engineering: A 392(1-2) (2005) 106-111.

[17] S. Wu, X. Liu, Y.L. Chan, C.Y. Chung, P.K. Chu, C.L. Chu, K.O. Lam, K.W.K. Yeung, W.W. Lu, K.D.K. Luk, K.M.C. Cheung, In vitro bioactivity and osteoblast response on chemically modified biomedical porous NiTi synthesized by capsule-free hot isostatic pressing, Surface and Coatings Technology 202(11) (2008) 2458-2462.

[18] G. Chen, P. Cao, G. Wen, N. Edmonds, Y. Li, Using an agar-based binder to produce porous NiTi alloys by metal injection moulding, Intermetallics 37 (2013) 92-99.

[19] M.H. Ismail, R. Goodall, H.A. Davies, I. Todd, Porous NiTi alloy by metal injection moulding/sintering of elemental powders: Effect of sintering temperature, Materials Letters 70 (2012) 142-145.

[20] B. Zhu, D. Li, C. Du, Z. Wan, Y. Zhou, C. Shu, F. Luo, Y. Li, Near-spherical micron-porous NiTi alloys with high performances fabricated via metal injection molding, Materials Science and Engineering: A 892 (2024).

[21] X. Wang, S. Xu, S. Zhou, W. Xu, M. Leary, P. Choong, M. Qian, M. Brandt, Y.M. Xie, Topological design and additive manufacturing of porous metals for bone scaffolds and orthopaedic implants: A review, Biomaterials 83 (2016) 127-141.

[22] T.C. Dzogbewu, D.J. de Beer, Additive manufacturing of NiTi shape memory alloy and its industrial applications, Heliyon 10(1) (2024).

[23] H. Ibrahim, A. Jahadakbar, A. Dehghan, N. Moghaddam, A. Amerinatanzi, M. Elahinia, In Vitro Corrosion Assessment of Additively Manufactured Porous NiTi Structures for Bone Fixation Applications, Metals 8(3) (2018).

[24] M.J. Ashrafi, A. Amerinatanzi, Z. Saebi, N. Shayesteh Moghaddam, R. Mehrabi, H. Karaca, M. Elahinia, Shape memory response of cellular lattice structures: Unit cell finite element prediction, Mechanics of Materials 125 (2018) 26-34.

[25] M. Speirs, B. Van Hooreweder, J. Van Humbeeck, J.P. Kruth, Fatigue behaviour of NiTi shape memory alloy scaffolds produced by SLM, a unit cell design comparison, J. Mech. Behav. Biomed. Mater. 70 (2017) 53-59.

[26] L. Yang, Y. Li, Y. Chen, C. Yan, B. Liu, Y. Shi, Topologically optimized lattice structures with superior fatigue performance, International Journal of Fatigue 165 (2022).

[27] Z. Chen, B. Wu, X. Chen, Y.M. Xie, Energy absorption and impact resistance of hybrid triply periodic minimal surface (TPMS) sheet-based structures, Materials Today Communications 37 (2023).

[28] E.F. Lehder, I.A. Ashcroft, R.D. Wildman, L.A. Ruiz-Cantu, I. Maskery, A multiscale optimisation method for bone growth scaffolds based on triply periodic minimal surfaces, Biomechanics and Modeling in Mechanobiology 20(6) (2021) 2085-2096.

[29] S. Saghaian, A. Amerinatanzi, N. Moghaddam, A. Majumdar, M. Nematollahi, S. Saedi, M. Elahinia, H. Karaca, Mechanical and shape memory properties of triply periodic minimal surface (TPMS) NiTi structures fabricated by selective laser melting. Biol, Eng. Med 3 (2018) 1-7.

[30] I. Maskery, N.T. Aboulkhair, A.O. Aremu, C.J. Tuck, I.A. Ashcroft, R.D. Wildman, R.J.M. Hague, A mechanical property evaluation of graded density Al-Si10-Mg lattice structures manufactured by selective laser melting, Materials Science and Engineering: A 670 (2016) 264-274.

[31] Z. Gorgin Karaji, M. Speirs, S. Dadbakhsh, J.-P. Kruth, H. Weinans, A. Zadpoor, S. Amin Yavari, Additively manufactured and surface biofunctionalized porous nitinol, ACS applied materials & interfaces 9(2) (2017) 1293-1304.

[32] X. Sun, F. Jiang, D. Yuan, G. Wang, Y. Tong, J. Wang, High damping capacity of AlSi10Mg-NiTi lattice structure interpenetrating phase composites prepared by additive manufacturing and pressureless infiltration, Journal of Alloys and Compounds 905 (2022).

[33] L. Sun, K. Chen, P. Geng, Y. Zhou, S. Wen, Y. Shi, Mechanical and shape memory properties of NiTi triply periodic minimal surface structures fabricated by laser powder bed fusion, Journal of Manufacturing Processes 101 (2023) 1091-1100.

[34] X. Yang, Q. Yang, Y. Shi, L. Yang, S. Wu, C. Yan, Y. Shi, Effect of volume fraction and unit cell size on manufacturability and compressive behaviors of Ni-Ti triply periodic minimal surface lattices, Additive Manufacturing 54 (2022).

[35] D. Lin, C. Zhang, X. Chen, N. Wang, L. Yang, TPMS_Scaffold_Generator: A Scaffold-Structure Generator Based on Triply Periodic Minimal Surfaces, Additive Manufacturing Frontiers 3(2) (2024) 200123.

[36] M. Zhang, Y. Yang, W. Qin, S. Wu, J. Chen, C. Song, Optimizing the pinch-off problem for gradient triply periodic minimal surface cellular structures manufactured by selective laser melting, Rapid Prototyping Journal 26(10) (2020) 1771-1781.

[37] I. ISO, Mechanical testing of metals—ductility testing—compression test for porous and cellular metals, 2011, Google Scholar   (2011).

[38] L. Yang, C. Yan, W. Cao, Z. Liu, B. Song, S. Wen, C. Zhang, Y. Shi, S. Yang, Compression–compression fatigue behaviour of gyroid-type triply periodic minimal surface porous structures fabricated by selective laser melting, Acta Materialia 181 (2019) 49-66.

[39] Q. Han, H. Gu, R. Setchi, Discrete element simulation of powder layer thickness in laser additive manufacturing, Powder Technology 352 (2019) 91-102.

[40] L. Yang, Y. Li, S. Wu, P. Chen, H. Wu, J. Su, H. Wang, J. Liu, C. Yan, Y. Shi, Tailorable and predictable mechanical responses of additive manufactured TPMS lattices with graded structures, Materials Science and Engineering: A 843 (2022).

[41] M. Zhang, X. Fang, Y. Wang, X. Jiang, T. Chang, N. Xi, K. Huang, High superelasticity NiTi fabricated by cold metal transfer based wire arc additive manufacturing, Materials Science and Engineering: A 840 (2022).

[42] A. Amadi, M. Mohyaldinn, S. Ridha, V. Ola, Advancing engineering frontiers with NiTi shape memory alloys: A multifaceted review of properties, fabrication, and application potentials, Journal of Alloys and Compounds 976 (2024).

[43] R. Hedayati, M. Sadighi, M. Mohammadi-Aghdam, A.A. Zadpoor, Mechanics of additively manufactured porous biomaterials based on the rhombicuboctahedron unit cell, J. Mech. Behav. Biomed. Mater. 53 (2016) 272-294.

[44] S.-Y. Park, K.-S. Kim, B. AlMangour, D. Grzesiak, K.-A. Lee, Compressive deformation behavior and energy absorption characteristic of additively manufactured sheet CoCrMo triply periodic minimal surface lattices, Journal of Materials Research and Technology 18 (2022) 171-184.

[45] Z. Pu, D. Du, K. Wang, G. Liu, D. Zhang, H. Zhang, R. Xi, X. Wang, B. Chang, Study on the NiTi shape memory alloys in-situ synthesized by dual-wire-feed electron beam additive manufacturing, Additive Manufacturing 56 (2022).